



Coarse Sand Transport Processes in the Ripple Vortex Regime Under Asymmetric Nearshore Waves

N. Fritsch^{1,2} , G. Fromant¹, D. Hurther³, and I. Cáceres⁴ 

¹LISIC, Université du Littoral Côte d'Opale, Calais, France, ²Géo-Océan, Université de Bretagne Occidentale, Plouzané, France, ³LEGI, Université Grenoble Alpes, CNRS, Grenoble-INP, Grenoble, France, ⁴LIM/UPC, Universitat Politècnica de Catalunya, Barcelona, Spain

Key Points:

- Good agreement in terms of ripple shape, migration speed and net transport rate is found with U-tube studies realized under similar hydrodynamic and sediment conditions
- Pick up due to vortex entrainment on the stoss side is more important than on the lee side due to the acceleration skewed flow conditions
- Contrary to the velocity-skewed case, the net resulting ripple averaged transport is onshore directed

Correspondence to:

N. Fritsch,
noemie.fritsch@univ-brest.fr

Citation:

Fritsch, N., Fromant, G., Hurther, D., & Cáceres, I. (2024). Coarse sand transport processes in the ripple vortex regime under asymmetric nearshore waves. *Journal of Geophysical Research: Oceans*, 129, e2023JC020189. <https://doi.org/10.1029/2023JC020189>

Received 17 SEP 2023

Accepted 22 MAR 2024

Author Contributions:

Conceptualization: N. Fritsch
Data curation: N. Fritsch, I. Cáceres
Formal analysis: N. Fritsch, G. Fromant, D. Hurther
Funding acquisition: G. Fromant, D. Hurther
Investigation: N. Fritsch
Methodology: N. Fritsch, G. Fromant, D. Hurther, I. Cáceres
Project administration: G. Fromant, D. Hurther
Resources: N. Fritsch, G. Fromant, D. Hurther
Software: N. Fritsch
Supervision: G. Fromant, D. Hurther, I. Cáceres
Writing – original draft: N. Fritsch
Writing – review & editing: N. Fritsch, G. Fromant, D. Hurther

© 2024. The Authors.

This is an open access article under the terms of the [Creative Commons Attribution License](https://creativecommons.org/licenses/by/4.0/), which permits use, distribution and reproduction in any medium, provided the original work is properly cited.

Abstract Large-scale wave flume experiments are conducted in the ripple vortex regime to study near bed coarse sand transport processes below asymmetric surface waves typical of the coastal nearshore region. For this purpose, a set of complementary acoustic instruments were deployed under regular nearshore wave conditions. Time-resolved velocity, sand concentration and sand flux profiles are measured across both the dense bedload and dilute suspension layers with an Acoustic Concentration and Velocity Profiler. The equilibrium 2D suborbital ripples are in good agreement in terms of dimensions, shape and onshore migration rate with Wang and Yuan (2018, <https://doi.org/10.1029/2018jc013810>, 2020, <https://doi.org/10.1016/j.coastaleng.2019.103583>). Stoss ripple vortex entrainment around the trough-to-crest flow reversal (FR+) is found to be more energetic in terms of sand pick-up into suspension compared to the counter rotating lee side vortex around the FR- flow reversal, as a consequence of the onshore skewed wave acceleration. Ripple vortex driven nearbed velocity phase leads around both flow reversals exceed typical bed friction induced values found in turbulent Wave Boundary Layers. Intrawave sand erosion events can be distinguished locally at the two ripple vortex positions around the flow reversals and two events more uniformly distributed along the ripple profile at wave crest and trough. Spatial fields of sand flux reveal the origin of the net onshore directed suspended and bedload transport. Good agreement is found with the mechanism identified under asymmetric oscillatory flows in Wang and Yuan (2020, <https://doi.org/10.1016/j.coastaleng.2019.103583>). Differences with ripple vortex regime under skewed shoaling waves and symmetric oscillatory flows are highlighted.

Plain Language Summary Ripples are common bedform features on sandy beaches. They are formed under specific wave conditions and influence sand transport under waves. Indeed, when the wave passes over the wave crest, a vortex is created on the ripple flank. This modifies sand transport on beaches and makes it harder to predict. Predictions of sand transport on beaches are nevertheless extremely important to study long-term coastal evolution, which is crucial to solve social and environment issues. In this paper, ripple formation and transport under specific wave conditions are studied. Inside a ripple cycle, two flow reversals are present (i.e., the moments where the direction of the flow changes), and in this particular case, we focus on the waves for which the second flow reversal (from negative to positive flow velocity) happens much quicker than the first flow reversal (from positive to negative flow velocity). This influences the creation of the vortices above ripple flanks and therefore sand transport: indeed, it turns out that the vortex created on the offshore side of the ripple during the second flow reversal is more energetic and therefore leads to more sand transport in the onshore direction above the ripple than the other vortex.

1. Introduction

Coastal seabeds constituted of non-cohesive sediments are covered by a large diversity of bedforms with sizes ranging from several centimeters in length up to several tenths of meters. Such bedforms interact with the flow in many different ways and their quantitative prediction on the basis of physical process-based models remain a scientifically challenging task (Nielsen, 1988). In wave/current dominated environments, the type of equilibrium bedforms prevailing in a certain coastal area depends mainly on local nearbed flow and sediment properties including wave, current, sediment size and density parameters (Nielsen, 1992). In sandy nearshore regions, one of the most common equilibrium bedforms are periodic 2D shaped sand ripples aligned in the wave propagation direction (Figure 1b). These features with typical sizes on the order of $\mathcal{O}(10\text{cm})$ in height and up to $\mathcal{O}(100\text{cm})$ in length, are found to scale with the nearbed orbital motion driven by the local surface wave characteristics. When the steepness of sand ripples (expressed as the ratio η/λ of ripple height η over ripple length λ) exceeds a critical

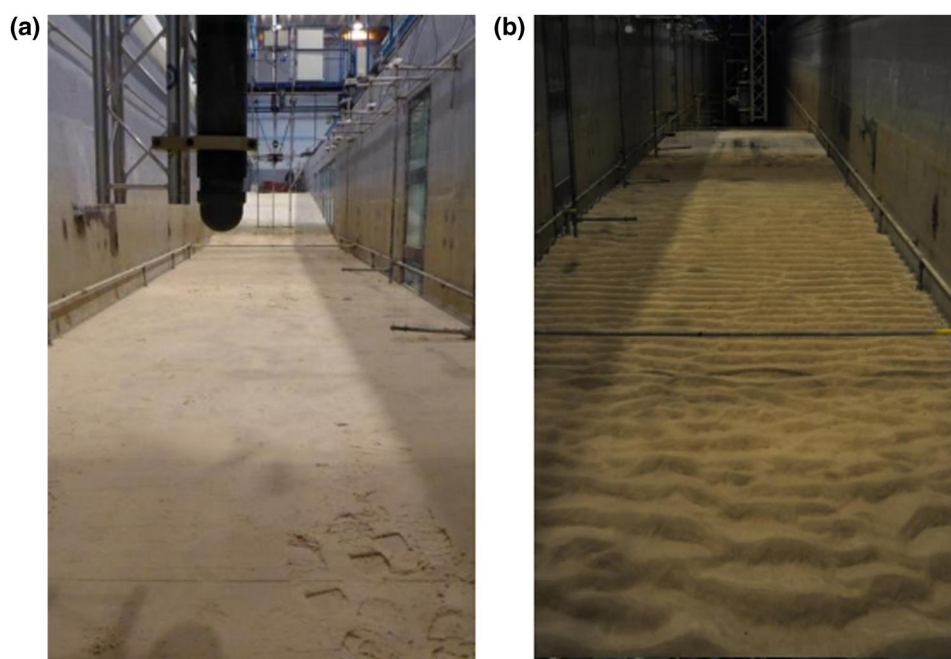


Figure 1. Study area (sandpit area) before (a) and after (b) a typical run.

value around 0.1, flow detachment occurs at wave crest and wave trough phases, on either side of the ripple crest generating ripple vortices on the alternating lee-faces at the origin of the so-called ripple vortex regime. These periodically produced two ripple vortices strongly affect the transport of sand by increasing the amount of suspended sand in contrast to regimes over flat sediment beds such as the more energetic sheet flow regime (Ribberink et al., 2008). The mechanism at the origin of the suspended sediment load is the so-called ripple vortex entrainment process associated with vortex shedding (for both ripple vortices) around the flow reversal following the flow detachment event on the lee wake region. This transport mechanism, also called the ripple vortex regime (Nielsen, 1992; Ribberink et al., 2008), has been investigated in detail over the past decades, from an experimental and modeling point of view (Bagnold, 1946; Davies & Thorne, 2005; Davies & Villaret, 1997; Earnshaw & Greated, 1998; Hurther & Thorne, 2011; Nichols & Foster, 2007; Sato & Horikawa, 1986; Sleath, 1984; Thorne et al., 2009; van der Werf et al., 2007; Wang & Yuan, 2018, 2020) with more and more performant flow measurement systems. The most advanced technologies provide turbulence-resolved measurements of co-located 2C/3C flow velocity, particle concentration and sand flux profiles, simultaneously across the dense bedload and dilute suspension layers using the Acoustic Concentration and Velocity Profiler technology (Fromant et al., 2018, 2019; Guta et al., 2022; Hurther et al., 2011; Naqshband et al., 2014; Revil-Baudard et al., 2015). From a numerical point of view, single- and two-phase flow-particle approaches have been implemented, such as DNS, LES with dynamic Smagorinsky-type subgrid-scale modeling and RANS simulations with more standard $k-\epsilon$ or $k-\omega$ turbulence closures (Amoudry et al., 2013; Malarkey & Davies, 2002; Salimi et al., 2020, 2021; Scandura et al., 2000; van der Werf et al., 2008).

In the case of symmetric waves and symmetric oscillatory flow conditions (used as proxies for Wave Boundary Layers in Oscillating Water Tunnels), the sand ripples do not migrate in the wave propagation direction and both ripple vortices entrain the same amount of sand into suspension with no difference between the opposite directed net sand transport rates linked to the two wave half-cycles. Under such symmetric flows, the presence of phase lagging effects (Ribberink et al., 2008), that is, when sand entrained into suspension in one wave half-cycle is transported in the following half-cycle, does not impact the net sand transport rate which remains negligibly low. In turn, coastal waves are subject to wave non-linearities in the nearshore region due to bed topography interactions under shallow water conditions (Ruessink et al., 2012). Two types of wave shape asymmetries prevail with significant differences in ripple vortex dynamics and in the coupled non-zero net sand transport rates: wave skewness and asymmetry. To see the characteristic shape of both types of waves, please refer to Wang and Yuan (2020), Figure 10, first line.

The most studied type of wave asymmetry concerns skewed waves characterized by sharp crests and long troughs typical of weakly skewed coastal sea waves propagating over nearly flat continental shelves with small sand ripples (η up to several centimeters) in moderately shallow waters (i.e., $0.1 < h_0/L < 0.5$ with h_0 and L as the local still water depth and the wavelength of surface waves, respectively). The hydrodynamics and sand transport for the case of skewed waves have been studied first on the basis of experiments conducted in small-scale Oscillating Water Tunnels and in large-scale wave flumes (Bijker et al., 1976; Davies & Thorne, 2005; Earnshaw & Greated, 1998; Nichols & Foster, 2007; Thorne et al., 2009; Thorne & Hanes, 2002; Villard et al., 2000). The case of strongly skewed waves studied herein, corresponds to nearshore shoaling and surf zone waves ($h_0/L < 0.1$) in presence of large sand ripples (η up to several tens of centimeters). The skewed wave case has been studied more and more over the past two decades, particularly in the context of abrupt climate change, all the more so since skewed waves have great influence on cross-shore sand transport rate controlling beach erosion, recovery, resilience as well as coupled coastline evolution. The strongly skewed case has been studied in details based on full-scale experiments and simulations of Oscillating Water Tunnel flows (Amoudry et al., 2013; Bijker et al., 1976; O'Donoghue et al., 2006; van der Werf et al., 2006, 2007, 2008; van der A et al., 2013; Salimi et al., 2020, 2021). In these studies, the wave shape skewness is simulated via an imposed value of the free-stream wave velocity skewness. An onshore directed net bedload transport is revealed with an offshore directed net suspended sand transport induced by the asymmetric contribution of ripple vortex entrainment. The total net sand transport rate was shown to vary with the magnitude of the offshore directed suspended sand transport. Van der Werf et al. (2007) showed that the suspended sand transport magnitude scales with the vortex suspension parameter $P = \eta/d_{50}$, with d_{50} as the median sediment diameter, and that for values of P above a critical range of 70–90, the total net transport rate is offshore directed due to the larger magnitude of the ripple vortex induced suspended transport compared to the onshore directed bedload transport (driving the onshore ripple migration). These results have recently been confirmed by advanced Eulerian two-phase fluid/particle simulations for sediment transport (Salimi et al., 2020) representing oscillatory boundary layer flow conditions, and had already been suggested much earlier in Nielsen et al. (1978). The onshore directed bedload sand flux and the resulting onshore ripple migration speed were in good quantitative agreement with the experimental results of van der Werf et al. (2007). As for the experiments, the numerical simulations confirmed a net offshore directed suspended sand flux due to the more energetic sand entrainment into suspension of the lee-side ripple vortex around the onshore-offshore (FR-) flow reversal. The unbalance between both vortices drives a higher offshore directed sand transport during the wave trough half-cycle than during the wave crest half-cycle because of less energetic ripple-vortex entrainment during the prior offshore-onshore (FR+) flow reversal. The magnitude of offshore directed net suspended sand flux was found to be underestimated by the numerical simulations, which was attributed to limitations of the implemented $k-\epsilon$ turbulence closure. For this purpose, turbulence-resolved LES are currently under development for improved numerical simulations of the suspended load in the ripple vortex regime (Zhang et al., 2022). Despite these small discrepancies, both experiments and simulations agreed on the bedload dominated onshore ripple migration and the asymmetric ripple vortex entrainment mechanism driving the net offshore directed suspended sand flux under strongly skewed oscillatory flows.

Because skewed oscillatory flows differ from skewed wave driven flows due to boundary layer streaming induced by asymmetric turbulence (Ribberink & Al-Salem, 1995; Trowbridge & Madsen, 1984) or by the non-zero vertical orbital velocity component (Kranenburg et al., 2012; Longuet-Higgins, 1953) as well as due to horizontal pressure gradient forces (Berni et al., 2013; Cheng et al., 2018; Foster et al., 2006; Sleath, 1999), Hurther and Thorne (2011) conducted rippled bed experiments under real shoaling waves in a large-scale wave flume for flow conditions similar to the strongly skewed oscillatory flows conditions in van der Werf et al. (2007). Asymmetric ripple vortex entrainment (in the sense of velocity skewness) was also identified as the driving mechanism of the net offshore directed suspended sand transport rate. Furthermore, the net onshore directed bedload sand transport rate was found to drive the onshore ripple migration but the net total sand transport rate was onshore directed rather than offshore directed as in the skewed oscillatory flows of van der Werf et al. (2007). One plausible explanation can be attributed to a larger contribution of net onshore directed bedload transport due to the nearbed onshore streaming occurring under shoaling waves.

The second type of wave asymmetry concerns waves characterized by an onshore leaned shape as so-called sawtooth waves associated with an onshore skewed acceleration rather than an onshore skewed velocity (for the so-called skewed wave case). This case is typical of nearshore waves with a maximum asymmetry magnitude in the surf zone. Insight into sand transport under asymmetric waves is available in King (1991) and

Nielsen (1992). Only recently, the ripple vortex regime under strong asymmetric oscillatory flows was addressed by Wang and Yuan (2020) for coarse sand experiments. They revealed a net onshore directed sand transport rate induced by an asymmetric ripple vortex entrainment process. Contrary to the strongly skewed oscillatory flow and strongly skewed shoaling wave cases, the (onshore counter-clockwise rotating) stoss-side ripple vortex entrainment around the FR+ flow reversal was observed to be more energetic than the (offshore clockwise rotating) lee-side ripple vortex entrainment around the FR- flow reversal. This contributed to a net onshore directed suspended sand transport rate over (bedload dominated) onshore migrating ripples denoting a slightly steeper (offshore) stoss-face with the presence of characteristic elongated ripple trough zones on either side of the ripple crest.

In this present study, only the coarse sand case is studied (coarse sand corresponding to a median grain diameter greater than 0.400 mm). Shimamoto (2016) shows the influence of sand grain size on transport behavior in the reference frame of different rippled beds and various hydrodynamic conditions, mostly with Figures 3–1 (page 49 from Shimamoto, 2016). This study shows that offshore transport occurs for high velocity skewness in the fine sand case, whereas offshore transport occurs for low asymmetry in the coarse sand case. On the contrary, onshore transport occurs for low velocity skewness in the fine sand case and for high acceleration skewness in the coarse sand case.

Just as for the strongly skewed wave case, the present study is focused on the effects of acceleration skewness under asymmetric nearshore waves in the ripple vortex regime for coarse sand experiments conducted in a large-scale wave flume. Whether the same ripple vortex dynamics and sand entrainment process are at the origin of the suspended sand transport observed in the strongly asymmetric oscillatory flow experiments of Wang and Yuan (2020) will be addressed in detail. For this purpose, the paper first describes the experimental setup and flow conditions including a comparative analysis of the measured ripple dimensions, shape, migration speed and the total net sand transport rate separated into suspension and bedload contributions. The results part addresses the detailed ripple vortex dynamics and its impact on the velocity, concentration and sand flux fields at intrawave scale and in mean, along the ripple cross-shore profile. In the last part, the differences with the coarse sand ripple vortex regime under symmetric, strongly skewed oscillatory flows and skewed waves are put into quantitative evidence on the basis of a comparison to the recent simulation results obtained by Salimi et al. (2020, 2021).

2. Experimental Setup and Flow Conditions

2.1. Experimental Protocol and Flow Instrumentation

The experiments were conducted in the CIEM wave flume of UPC Barcelona within the European Hydralab+ project RIPCOM from September 2017 to January 2018. This large-scale facility of 100 m long, 3 m wide and 4.5 m deep, allows full-scale wave experiments with real sand mixtures constituting the granular flow bed. The bed profile of the flume starts with a 35 m long horizontal concrete bed in the deepest offshore part (with a still water depth set to 2.65 m), followed by a 17-m-long 1:12 slope concrete bed, up to an 18-m-long horizontal section composed of a concrete bed over the first 4 m and a 14-m-long sandpit corresponding to the study area (Figure 1). The sand pit is represented with a drawing on Figure 2, with a zoom on the representation of our study area at the top of Figure 2. The still water depth in the sandpit area is 1 m inducing non-breaking progressive waves in the studied regular wave conditions (described in the following section). The sandpit is filled with a unimodal coarse sand of median diameter $d_{50} = 0.545$ mm ($d_{10} = 0.321$ and $d_{90} = 0.794$ mm). After the study area, a rigid bed parabolic dissipative profile is set up with an average slope of 1:7 up to a final 1:50 section that goes beyond the run-up wave.

Waves are generated by a wedge-type paddle at the offshore deep-water end of the flume allowing nearly full-scale surface wave conditions. The experimental protocol consisted of an initial horizontal flattening of the sand bed over the entire sandpit length (Figure 1a) before waves are started during 2 hours long runs of regular waves (see Figure 1b for an example of resulting rippled bed). The splitting into two runs allows an eventual repositioning of the flow instruments mounted on a moveable platform (described in the following paragraph). The first 50 min of the first run permits establishment of equilibrium sand ripples of constant dimensions. These first 50 min of transients are discarded from the present analysis focusing on wave-induced ripple vortex processes at morphological equilibrium states.

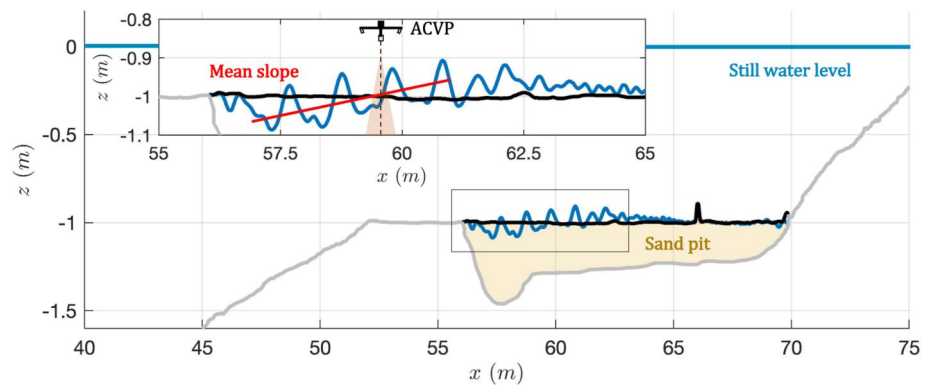


Figure 2. Representation of the flume bed profile evolution and the studied sand pit area (brown colored zone). The gray, black and blue solid curves in the sand pit area represent the rigid concrete bed, the initial horizontal sand bed (before the start of the experiment) and the final rippled sand bed (after the 2×2 h long experiments). In the zoomed panel, the mean bed slope (red line) and the ACVP cross-shore position are shown.

Figure 3a shows the set of flow instruments mounted on the movable platform which was positioned in cross-shore (with a ± 1 cm accuracy) and vertical (with a ± 1 mm accuracy) directions along the sand pit area before the start of each run. One ADV (Nortek Vectrino) was placed 5 cm below the wave trough to measure the free stream velocity above the ripple. A Bedform And Suspended Sediment Imager (BASSI) (Moate et al., 2016; Thorne et al., 2018) was used to track the bedform evolution during the wave runs over a 1.5 m long cross-shore transect and to estimate the net sand transport rate from an Exner sediment mass balance method. Wave height was obtained from a piezo-electrical pressure transducer (PPT) fixed on the trolley. Finally, an Acoustic Concentration and Velocity Profiler (ACVP) was mounted on the trolley to measure time-resolved vertical profiles of the velocity field, sand concentration and detected bed position over a maximal profiling depth of 20 cm above the detected sand bed (see Figure 3b). The ACVP is mounted above the sand pit (study area), as is shown on Figure 2. At the end of each run, three acoustic echosounders (one at the flume's centerline and the two others at 1 m on either side) mounted on a separate moveable trolley recovered the cross-shore bed profiles over the entire sandpit area.

The data collected with the ACVP system will be the main focus of this study. This device combines incoherent acoustic particle scattering theory for sand concentration profiling and pulse-to-pulse coherent Doppler velocity estimation for 1D vertical profiling of 2C (two components u, w) velocity (Fromant et al., 2018; Hurther et al., 2011; Thorne & Hurther, 2014) at a temporal resolution of 70 Hz. Because sand concentration and velocity are measured simultaneously within the same sample volume (of about 50 mm^3 locally), sand flux profiles are quantified at turbulent scales ($\mathcal{O}(1 \text{ mm}, 10 \text{ ms})$). This advanced hydro-acoustic flow sensing technology has been successfully applied over the past 10 years to investigate turbulent boundary layer sediment transport processes associated with suspension and bedload transport (Fromant et al., 2019; Hurther & Thorne, 2011; Naqshband et al., 2014, 2017; Revil-Baudard et al., 2015; Zomer et al., 2021). In this study, velocity, sand concentration and sand flux data are separated into bedload and suspended load contributions using the time-resolved tracking of the suspension and detected flow bed interfaces. The suspension interface corresponds to the height closest to the 8% threshold value in volumetric particle concentration (Ribberink et al., 2008). Below this commonly applied threshold value, particle-particle interactions due to binary particle collisions and granular friction can be neglected. The bed is detected with the ABIT method (Fromant et al., 2018; Hurther & Thorne, 2011). The decomposition of all measured quantities into periodic wave- (also called orbital component in oscillatory flows) and (mean) current-driven components is done following the methods proposed in Hurther and Thorne (2011) and Fromant et al. (2019).

2.2. Wave Conditions and Sediment Transport Regime

The regular wave period, wave height and still water depth values in the test section of the flume are $H_o = 30 \text{ cm}$, $T = 9 \text{ s}$, and $h_o = 2.65 \text{ m}$ (Table 1). The onshore propagating surface gravity waves led to the formation of 2D sand ripples (see Figure 1b) under non-breaking waves in the studied sand pit area. Figure 4 shows the free-stream wave velocity (measured by the ADV above the ripple and WBL influenced region) at the studied sand pit

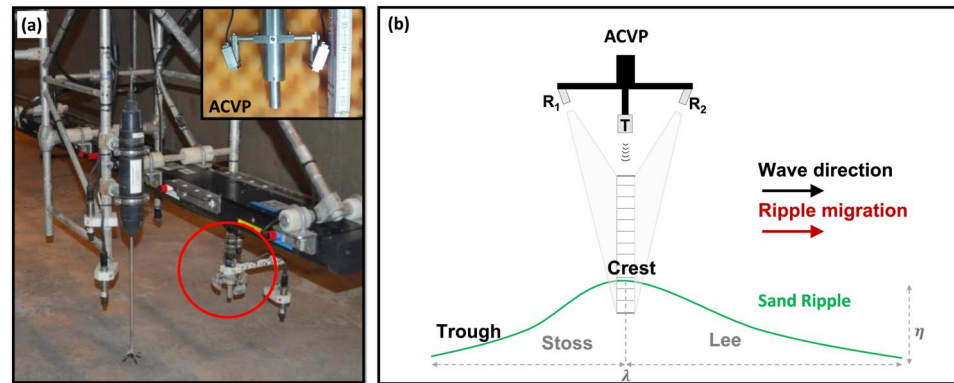


Figure 3. (a) Set of flow instrumentation (ACVP, BASSI, ADV and PPT sensors) mounted on the movable trolley in the study area (sandpit area). (b) Positioning of ACVP above an onshore migrating sand ripple.

position located at $x = 59$ m onshore from the wave paddle. At this location, the root mean square wave velocity is $u_{rms} = 0.4$ m/s with a first and second harmonic velocity amplitude of $u_1 = 0.1$ m/s and $u_2 = 0.027$ m/s. The orbital diameter based on the u_{rms} velocity is $D_0 = \frac{\sqrt{2}u_{rms}T}{\pi} = 0.8$ m (orbital excursion). This value and the Reynolds number $Re = \frac{\sqrt{2}u_{rms}D_0}{\nu} = 4 \times 10^5$ reveal the nearly full-scale wave and fully established turbulent flow conditions in the studied sandpit area. The wave velocity skewness and the wave acceleration skewness are $R = \frac{u_{max}}{u_{max} - u_{min}} = 0.51$ and $\beta = \frac{a_{max}}{a_{max} - a_{min}} = 0.64$, respectively, where u_{max} , u_{min} and a_{max} , a_{min} are the maximum and minimum wave velocity and wave acceleration, respectively, over the wave cycle. It can be deduced that the waves are mainly asymmetric (acceleration skewed) with negligible velocity skewness, associated with a sawtooth wave shape as can be seen in Figure 4. The wave parameter $\alpha = 0.27$ is the value of the ratio between the first and second harmonic wave velocity amplitudes obtained from a Fourier decomposition of the free-stream wave velocity signal. This value, together with the R - and β -values, are in good agreement with the oscillatory flow cases tested by Wang and Yuan (2020) for purely acceleration skewed wave velocity with an α and β pair value of 1/6 and 0.65, respectively. Furthermore, the values of the wave period, velocity and water excursion amplitudes suggest conditions very close to their Td_060b case (see Table 1 for comparison). As a consequence, the results found here under acceleration skewed surface gravity waves will be compared to those obtained under idealized acceleration skewed oscillatory flows in Wang and Yuan (2020).

The sediment transport regime is first determined with the value of the dimensionless mobility number Ψ for the studied coarse sand case of median diameter $d_{50} = 545$ μ m. A value of $\Psi = \frac{u_{max}^2}{(s-1)g.d_{50}} = 41$ is obtained with u_{max} as the maximum wave velocity over the wave cycle, $s = 2.65$ the specific sand density and g the gravitational acceleration. As expected, the Ψ value lies in the bedform regime well below the critical value for sheet flow conditions (O'Donoghue et al., 2006).

3. Ripple Characteristics

3.1. Ripple Dimensions and Type

Table 2 indicates the dimensions of the sand ripples obtained at equilibrium stage (after the first 50 min of the first run) with the echosounder measurements for the present experiment (first line, last columns). As previously shown by O'Donoghue et al. (2006) under similar oscillatory flow conditions, the use of a coarse sand with a d_{50}

Table 1
Experimental Flow Forcing Conditions (Free Stream) for Our Present Experiment (First Line) and Wang and Yuan Experiment (second Line of the Table)

Parameter	$T(s)$	$h_0(m)$	$H_0(m)$	$u_{rms}(m/s)$	$u_1(m/s)$	$u_2(m/s)$	$D_0(m)$	Re	β	R	α
Present experiment	9	2.65	0.3	0.4	0.1	0.027	0.8	4×10^5	0.64	0.51	0.27
Wang and Yuan (2020)	8.33	x	x	x	x	x	0.79	$4 \times 74 \cdot 10^6$	0.65	0.50	0.25

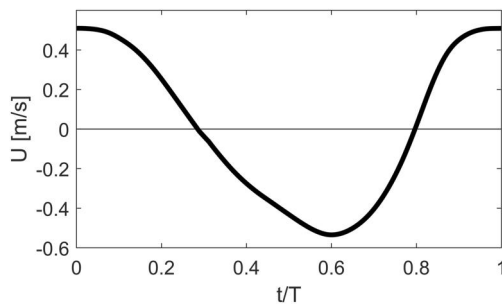


Figure 4. Free-stream wave velocity at the studied sand pit position measured by the ADV.

value above 300 μm induces the generation of 2D ripples composed of long crestlines (much longer than the ripple length in cross-shore direction) in longshore direction. Using the ripple classification proposed by Widberg and Harris (1994) in wave dominated flows, we obtain a ratio value $D_0/d_{50} = 2,000$ corresponding to ripples in the suborbital regime. The ripple height and length values $\eta = 0.13$ m and $\lambda = 1$ m, further confirm the good agreement with the acceleration skewed oscillatory test named Td_060b in Wang and Yuan (2020). The ripple height over length ratio $\eta/\lambda = 0.13$ is above critical threshold value of 0.1 suggesting established ripple vortex regime associated with flow detachment and counter rotating ripple vortices generated at specific phases in the wave cycle on either side of the ripple crest (analyzed in details in Section 3.1). A more detailed analysis proposed by Wang and Yuan (2020) of acceleration skewness induced effects on the mean

ripple dimensions consists in evaluating the normalized ripple length λ/λ_{sin} , height η/η_{sin} and ratio $(\eta/\lambda)/(\eta_{sin}/\lambda_{sin})$ taking as the normalization quantity the ripple length, height and ratio obtained under sinusoidal (i.e., symmetric) oscillatory flow conditions (when $\alpha = 0$). For this purpose, the symmetric flow ripple dimensions obtained by Wang and Yuan (2020) in test Td060_0 ($\lambda_{sin} = 864$ mm, $\eta_{sin} = 165$ mm, $\eta_{sin}/\lambda_{sin} = 0.19$) are used here for the symmetric wave case (since such tests cannot be carried out with real surface waves in wave flume experiments subject to inherent wave shape transformation along the nearshore zone). The values of the normalized ripple dimensions and slope obtained here for asymmetric waves are compared to the results of Wang and Yuan (2020) for test Td060_b (as the closest in terms of wave conditions, wave asymmetry degree $\alpha = 1/4$ and sand properties). Comparison between values from our experiment and from Wang and Yuan (2020) U-tube experiment is made in Table 2. As for acceleration skewed oscillatory flows, we find that the normalized ripple length and height are increased and decreased by a factor of roughly +13% and -19%, respectively. This induces a decrease of the normalized ratio $(\eta/\lambda)/(\eta_{sin}/\lambda_{sin})$ of about -25% for $\alpha = 1/4$. The similar tendencies for all three ripple size parameters strongly suggest similar acceleration skewness induced effects on the ripple dimensions under progressive nearshore waves.

3.2. Ripple Shape

In order to analyze the detailed ripple shape characteristics at equilibrium, a typical ripple profile, obtained with the echosounders at the end of the two-hour run is displayed in Figure 5. This curve reveals a fairly symmetric ripple shape with two elongated ripple troughs on either side of the ripple crest containing small humps. The mean slope values on the main offshore and onshore ripple faces are 0.3 and 0.275, respectively (the slopes are computed as the ratio of the height and the distance between the trough and the crest of the ripple, on the studied side - offshore or onshore). These values are well above the critical slope value of 0.1 for the initiation of ripple vortices on either side of the ripple crest. Wang and Yuan (2020) obtained very similar ripple shape characteristics for their asymmetric oscillatory flow conditions (fairly symmetric ripples with elongated troughs containing small irregular humps) contrary to their symmetric oscillatory flow cases approaching nearly sinusoidal ripple shapes. This suggests similar morphological effects of wave acceleration skewness and oscillatory flow acceleration skewness on ripple shape.

Furthermore, it can be seen in Table 2 that the slopes of the main offshore and onshore ripple faces are not exactly equal with a slightly higher value on the offshore side. It was previously shown in the literature that steeper faces are usually obtained on the onshore ripple face under velocity skewed oscillatory flows (van der Werf et al., 2007) and velocity skewed surface waves (Hurther & Thorne, 2011). In both cases, the steeper onshore face was explained by a more energetic onshore ripple vortex and associated onshore ripple vortex sand entrainment compared to the offshore ripple vortex dynamics. The analysis of the ripple vortex dynamics in Section 5.1 will look into these aspects in details.

3.3. Ripple Migration and Net Sand Transport Rate

Ripple migration direction and speed are determined from the analysis of the sand bed elevation data measured with the BASSI instrument during the morphological equilibrium phase (i.e., after the first 50 min of experiment duration). The suborbital equilibrium ripples are found to migrate in onshore direction at a constant speed of 1.56×10^{-4} m/s. This low value confirms that morphological velocity scales are more than three order of

Table 2
Coarse Sand Ripple Characteristics and Net Sand Transport Values for Our Present Experiment (First Line) and Wang and Yuan Experiment (second Line)

Parameter	Ψ	$\eta(m)$	$\lambda(m)$	S_{lof}	S_{lon}	d_{50} (μm)	S^p	Φ_{L_BASSI} (m^2/s)	Φ_{L_ACVP} (m^2/s)	Φ_{S_ACVP} (m^2/s)	Φ_{BL_ACVP} (m^2/s)	C_b (m/s)	η/λ	$\frac{n}{n_{lim}}$	λ/λ_{syn}	$(\eta/\lambda)/(\eta_{crit}/\lambda_{syn})$	C_b^*
Present exp.	41	0.13	1	0.32	0.27	545	2.6	1.3×10^{-5}	1.4×10^{-5}	5.7×10^{-6}	8.4×10^{-6}	1.56×10^{-4}	0.13	0.79	1.16	0.68	0.0014
Wang and Yuan (2020)	x	0.158	0.875	x	x	510	0	1.53×10^{-5}	1.53×10^{-5}	x	x	3.456×10^{-4}	0.18	0.91	1.02	0.9	0.0032

magnitudes lower than the wave-driven flow velocity scales. In order to compare the ripple migration speed to values reported in the literature under similar flow conditions, the normalized speed proposed in Wang and Yuan (2020) is estimated as $C_b^* = C_b \cdot T/\lambda$. We obtain $C_b^* = 0.0014$ revealing that it takes locally hundreds of wave periods for the ripple to migrate by one ripple length. This value is compared to $C_b^* = 0.0032$ in Wang and Yuan (2020) obtained for test case Td060_b as the closest acceleration skewed oscillatory flow condition. The more than two times lower onshore migration speed in the present surface wave case (for very similar forcing conditions) might be explained by the positive mean bedslope of about $Sl = 2.6^\circ$ found here in the studied sandpit area (see Table 2). The mean bedslope appears naturally under the effect of the progressive wave shape transformation along the nearshore domain. Wang and Yuan (2018) have shown in OWT experiments under symmetric oscillatory flow conditions that a mean bedslope in the range $0-3^\circ$ induces ripple migration and a net sand transport rate in the downslope direction. In the present case of a mean bedslope acting in opposite direction to the wave-induced ripple migration, the ripple onshore migration speed should be reduced compared to the value obtained in Wang and Yuan (2020) in (horizontal) Oscillatory Water Tunnel experiments.

Determination of accurate net sand transport rate values is of primary importance in sediment transport studies. Because this quantity is often subject to large measurement uncertainties (even in controlled laboratory experiments), two different methods relying on strictly independent measurements are used here to gain confidence in the estimated values of the net sand transport rate. The first method consists of resolving the well-known Exner mass balance equation using bathymetrical surveys obtained under steady wave forcing conditions in the closed flume experiments (Van der Zanden et al., 2017). This method is applied here to the bathymetrical surveys measured with the BASSI instrument (Φ_{tot_BASSI}). The second method uses a novel sand flux profiling approach, which is the product of the simultaneously measured time-resolved velocity and sand concentration profiles along the entire equilibrium ripple profile. These sand flux profiles are subsequently integrated vertically from the detected bed level to the top of the suspension layer (i.e., including the dense bedload layer) and finally time-averaged to form the net sand transport rate (Φ_{tot_ACVP}). Table 2 contains the net sand transport rates obtained with the two experimental methods. Both values are in close agreement in terms of sand transport direction as an onshore oriented mass flux, and agree in magnitude with a less than 10% higher value estimated by the ACVP measurement. When compared to the net sand transport rate obtained by Wang and Yuan (2020) in their similar coarse sand ($d_{50} = 510$ mm) experiments for nearly identical oscillatory flow conditions (test Td060_b), a slightly higher onshore oriented net sand transport rate of $1.53 \times 10^{-5} m^2/s$ was obtained in the horizontal OWT tests. The 10% lower sand transport rate found here under real progressive waves might be due to the small upward bed slope observed in the sandpit area (discussed in the previous paragraph). Finally, using the full measurement potential of the ACVP technology, the net sand transport rate associated with bedload (Φ_{BL_ACVP}) and suspended (Φ_{susp_ACVP}) sand transport are calculated separately by limiting the vertical integration range of the sand flux profile to the corresponding layers. The values in Table 2 show that both the bedload and suspended net sand transport rates are onshore oriented with a 20% higher contribution associated with bedload transport. Please note that the onshore oriented net suspended sand transport found here for asymmetric waves differs strongly from the typical offshore oriented suspended sand transport rate found for typical onshore skewed oscillatory flows (Van der Werf et al., 2007) and for typical onshore skewed shoaling waves (Hurther & Thorne, 2011). The underlying physical flow and sand entrainment mechanisms will be investigated in details below.

4. Data Processing Method and Data Set Nomenclature

This subsection explains the processing steps and methods applied to the ACVP and ADV data and defines the corresponding data nomenclature used for the data interpretation in Section 3. As explained in Section 2.1, the ACVP measurements were made at a fixed position in the shoaling zone of the channel providing Eulerian measurements of velocity, sediment concentration and bed interfaces positions with respect to z and time. The data discussed below focuses on the analysis of these measured quantities over a period of time corresponding to the onshore migration of an entire ripple profile beneath the ACVP (following the same methodology as Hurther and Thorne (2011)).

The *Local Time-Resolved Profiles (LTRP)* shown in the central 3D data set in Figure 6 corresponds to the re-arranged raw ACVP profiles shown for the concentration (colourplot) and the superimposed 2C-uw velocity vector fields. To get the re-arranged LTRP 3D-dataset shown in Figure 6, the wave velocity at the free-stream

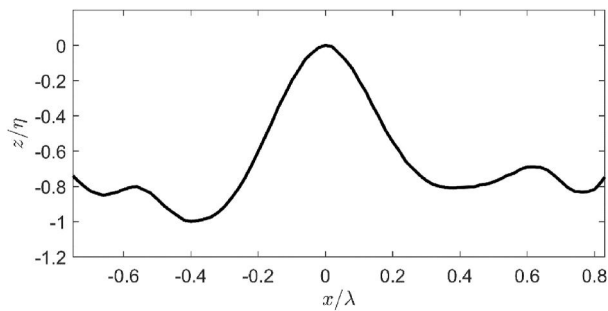


Figure 5. Averaged ripple profile obtained with the echosounders.

height (i.e., well above the WBL and ripple influenced nearbed region) must first be determined as a function of the wave period normalized intrawave phase t/T . For this purpose, a wave-by-wave decomposition of the velocity timeseries is done using a standard cross-correlation technique. Averaging over the number of waves and subtracting the mean (current-induced) velocity component gives the free-stream wave velocity shown in Figures 4 and 6. Intrawave phase $t/T = 0$ is taken at maximal onshore wave velocity at the wave crest. Within the wave cycle, four events are defined at specific intrawave phases with the following abbreviations: Wave Crest (WC), Wave Trough (WT), onshore/offshore Flow Reversal (FR-) and offshore/onshore Flow Reversal (FR+). The second processing step determines the cross-shore range (in x -direction) by matching the length of the selected sand ripple (shown in Figure 6 along the x -direction). Please note that because the ACVP

is positioned at a fixed cross shore position in the wave flume, the conversion of the ACVP acquisition time into cross-shore position x along the selected ripple, requires a measurement of its migration direction and speed with the BASSI instrument. This dimension corresponds to the ripple length normalized intra-ripple position x/λ in Figure 6. The positions $x/\lambda = 0$ and $x/\lambda = 1$ are taken at the ripple trough on the stoss-side (lowest detected bed elevation on the offshore ripple face) and at the ripple trough on the lee-side (lowest detected bed elevation on the onshore ripple face). Another specific location along the ripple profile is the ripple crest (highest detected bed elevation along the ripple profile) defined as the origin along the third dimension of the LTRP transect corresponding to the ripple height η normalized distance from the ripple crest z/η .

The *Intraripple phase-averaged Profiles (IrP)* is a 2D-dataset along the ripple profile x/λ resulting from the averaging along the intrawave dimension t/T of the LTRP data set. It is shown in Figure 6 for the sand flux quantity (colourplot) as the local product of the LTRP velocity and sand concentration.

The *Intrawave ripple-averaged Profiles (IwP)* is a 2D-dataset versus phase t/T resulting from the averaging along the ripple profile of the LTRP data set. It is shown in Figure 6 as the colourplot of the horizontal wave velocity component u .

The *Intrawave Bedload integrated (IwB)* and *Intrawave Suspension integrated (IwS)* data sets are 1D as a function of phase t/T resulting from the vertical integration of the LRP data set of a given measured quantity (velocity, sand concentration or flux) over the bedload and suspension layer, respectively, and subsequent averaging along x . Examples for these data sets are shown in Figure 6 for the horizontal sand flux quantity.

The *Net Profile (NetP)* is a bed-referenced 1D data set as a function of z/η resulting from the averaging along the ripple profile of the IrP data set for a given measured quantity (taken as the horizontal sand flux in Figure 6).

The *Net, Net Bedload (NetB)* and *Net Suspension (NetS)* data sets are values (i.e., OD) of a given quantity (as the sand flux in Figure 6) resulting from the vertical integration over the entire vertical range z/η , the bedload layer and suspension layer, respectively, of the NetP data set. Please note that the NetB and NetS data sets can also be obtained from the averaging over the phase t/T of the IwB and IwS data sets, respectively. The Net data set is then equal to the sum of the NetB and NetS values.

5. Results

5.1. Ripple Vortex Dynamics

Flow detachment induced ripple vortices on either side of the ripple crest are known to play a dominant role in momentum and sediment transfers in the nearbed region, including both bedload and suspension layers. How this complex flow-sediment interaction process is related to the local free-stream wave (root mean square wave velocity magnitude, skewness and asymmetry) and current quantities (undertow and streaming induced), is of crucial importance for its proper parametrization in process-based sediment transport models. This section investigates the presence of lee- and stoss-side ripple vortices and their potential sand entrainment capacity via the representation in Figure 7, of the LTRP data sets for the 2C-uw velocity vector, sand concentration and horizontal sand flux along an entire ripple length λ at specific phases in the wave cycle. Figure 7a shows the free-stream wave velocity cycle with these specific phases as capital letters. Below, the corresponding colourplots of sand concentration and superimposed 2C velocity vector field are displayed in the same panels (3 plots of the first row).

Then, the corresponding colourplots of the horizontal sand flux are displayed in the second row. Following the methodology applied in Hurther and Thorne (2011), all LTRP data have been averaged over eight consecutive waves in order to reduce time and spatial variability associated with turbulence. Please note that during this averaging time interval, the ripple migrates over a cross-shore distance of about 11 mm in onshore direction which is considered as negligible with respect to the ripple length ($\lambda = 1$ m) and to the size of the ripple vortices scaling with the ripple height ($\eta = 0.13$ m). Sensitivity tests to the averaging time showed that no spatial distortion of the 2D figures was observed for an averaging over eight consecutive waves. In all plots of Figure 7, the thick solid and dashed black lines represent the positions of the detected bed level and of the lower suspension interface (as defined in Section 2.1).

Wave crest and trough: A, B, C sequences. The presence of ripple vortices on either side of the ripple crest is first checked on the basis of the 2C velocity and concentration fields at the wave crest (sequences A and C on Figure 7) and wave trough (sequence B on Figure 7) phases. Figure 8b is a zoom on the concentration contours and velocity field corresponding to sequence A (wave crest). It confirms the existence at the wave crest of a flow detachment zone characterized by typical S-shaped velocity profiles in the core of the vortex at $x/\lambda = 0.6$, induced by its clockwise rotation with an offshore-directed return flow just above the detected flow bed. Furthermore, Figure 8c shows the presence at the wave trough (sequence B) of a similar flow detachment process associated with an anti-clockwise rotating ripple vortex at $x/\lambda = 0.38$. The corresponding concentration fields on Figure 7b show that the ripple vortex regions at wave crest and trough are both associated with high suspended sand concentration values while on the opposite ripple face (with no ripple vortex), the sand is transported as a thin bedload layer. This further confirms high turbulent mixing subject to suspended sand transport in the vicinity of ripple vortices. No significant difference in terms of velocity and suspended sand concentration values are seen between the stoss- and lee-side ripple vortices at wave crest and trough phases. This supports the fact that under the present asymmetric surface wave conditions, the velocity magnitude at the wave crest and trough are very similar (contrary to onshore skewed shoaling waves or oscillatory flows inducing a more energetic lee-side ripple vortex compared to the stoss-side ripple vortex as shown in Salimi et al., 2021). The horizontal sand flux fields in Figure 7c reveal a clear dominance of sand transport as bedload at both wave crest and trough half-cycles with values up to $\pm 20 \text{ kg m}^{-2} \text{ s}^{-1}$. One particularly interesting feature of the sand flux colourplots is seen at the wave crest sequences A and C (Figures 8b and 8d) where the bedload sand flux in the lee-side vortex region is directed in the offshore direction due to the nearbed return flow associated with the flow detachment process. During the wave trough phase (sequence B), a ripple vortex induced return flow region with an onshore directed bedload sand flux cannot be distinguished, probably because the stoss-side ripple vortex is not yet fully established at phase B.

FR+ flow reversal: G, H, I sequences. The ability of the ripple vortices to entrain sand is verified around the flow reversal phases. For the FR+ reversal, the sand concentration fields in Figure 7f show the presence of a well delimited suspension cloud in the stoss-side ripple vortex region at phase G. This cloud is subsequently lifted up and advected in the onshore direction at phases H and I with concentration values up to 10 kg.m^{-3} . The sand flux colourplots around FR+ show the highest values as an onshore directed bedload transport in the well-delimited stoss-side ripple vortex region between $x/\lambda = 0.2$ and $x/\lambda = 0.4$ (0.5 for I sequence), which is due to high near bed shear stress values linked with strong flow acceleration (Nielsen, 1992) during FR+ reversal (Figure 7g). The sand flux values reached in the ripple vortex induced suspension cloud are an order of magnitude lower compared to the bedload layer values. Whether this observation is representative of the relative net suspended to bedload contributions will be addressed later using the IwB and IwS data sets.

FR- flow reversal: D, E, F sequences. The sand entrainment ability of the lee-side ripple vortex around the FR- reversal can be identified in Figure 7d but with a much less energetic contribution in terms of suspended sand concentration values compared to the FR+ event. The sand flux colourplots show low magnitude values homogeneously distributed along the ripple profile for all three sequences around the FR- reversal. As for the corresponding sequences around the FR+ reversal, the high flux values are observed in the bedload layer, between $x/\lambda = 0.6$ and $x/\lambda = 0.75$. Sand entrained around FR- reversal is subsequently transported as bedload in the offshore direction, however, with a lower magnitude than the onshore-directed bedload transport observed during and after FR+. This suggests that flow acceleration skewness induces bed shear stress asymmetry between wave crest and trough cycles leading to a net onshore ripple-averaged transport dominated by bedload. The intrawave dynamics are in good agreement with the net onshore sand transport measurements given in Table 1.

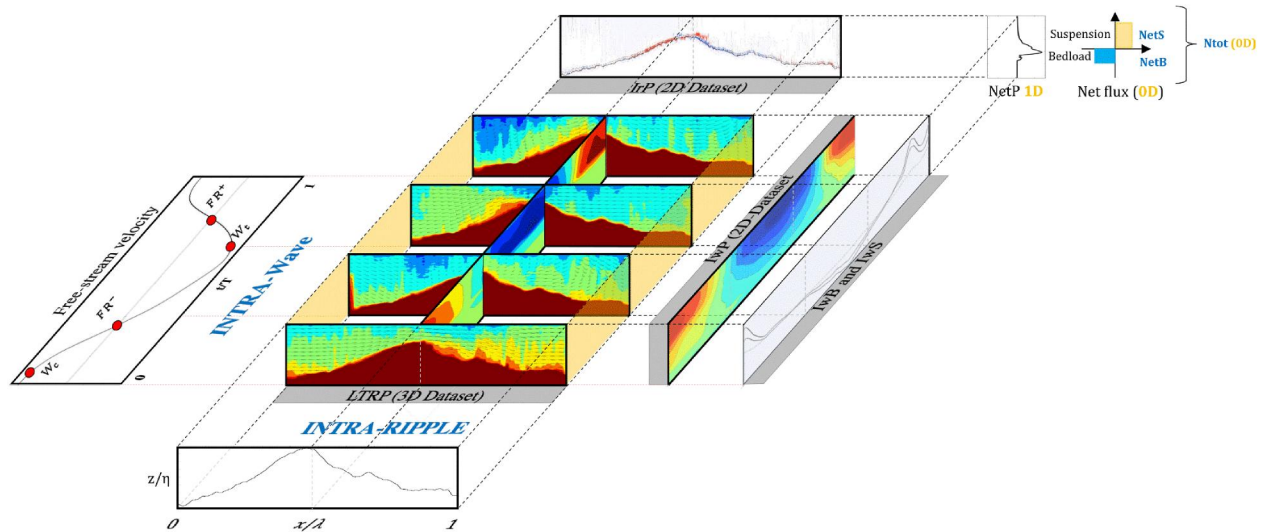


Figure 6. Split view of the typical data set recorded by the ACVP and associated derived products nomenclature used hereafter for the analysis: LTRP (Local-Time Resolved Profiles), IwP (Intrawave Profiles), IrP (Intra ripple Profiles), IwB (Intrawave Bedload) and IwS (Intrawave Suspension) data set.

It can be concluded from the LTRP data (Figures 7 and 8) that ripple vortices are generated on either side of the ripple crest at wave crest and trough phases but that the stoss-side ripple vortex entrains more sand in suspension around the FR+ reversal compared to the lee-side vortex around the FR- reversal. Furthermore, asymmetry in flow acceleration leads to higher bed shear stress during FR+ flow reversal, thus inducing a higher bedload transport in the onshore direction. No clear phase lagging effects could be detected in the LTRP data sets since the dominant sand entraining event associated with the short duration FR+ reversal is followed by the long duration onshore wave half-cycle over which the suspension sand cloud (seen at events D, H and I in Figure 7) has sufficient time to settle down. The sand entrainment around FR- is much less energetic (due to the much lower induced bed friction magnitude) with no well-defined suspended sand cloud and therefore no evidence of phase lagging. Finally, it appears that more sand is eroded at intrawave scale from the ripple stoss face which supports the slightly steeper slope value observed on the stoss side of the ripple in Section 3.2 (Figure 5).

5.2. Velocity Field

The present section focuses on the detailed velocity field characteristics in the nearbed region under an asymmetric nearshore wave condition forcing within the ripple vortex regime. Two specific aspects will first be considered (Figure 9), the local intrawave velocity (based on LTRP data sets) and the local mean velocity profiles (based on IrP data sets). These components were previously analyzed for oscillatory sheet flows (O'Donoghue & Wright, 2004) and in different types of oscillatory and wave driven flows in the ripple vortex regime (Hurther & Thorne, 2011; Salimi-Tarazouj et al., 2021; van der Werf et al., 2007) because of their relevance for reliable numerical modeling and predictions of intrawave and net sand transport rates. Finally, the mean concentration and velocity fields along the entire ripple profile (IrP data set) are investigated (Figure 10).

In Figure 9, the horizontal component of intrawave velocity colorplots are shown for the horizontal component at four different locations along the ripple profile noted as A (in the ripple trough), B (at the stoss-side ripple vortex position), C (at the ripple crest) and D (at the lee-side ripple vortex position). For each position, the vertical profiles of the phase shifts between the local and free-stream FR- event (solid black curve) and the local and free-stream FR+ event (dashed black curve) are displayed in the middle panels. Intrawave velocity plots were computed by averaging the velocity field over 20 consecutive waves around the specific position in order to reduce turbulence induced variability. The local phase shifts were computed by subtracting the phase of the corresponding flow reversal in the free stream velocity signal (measured with the ADV) from the phase in the local velocity signals measured with the ACVP profile. Therefore, positive and negative values of the phase shift ϕ (given in degree unit in the middle panels) correspond to phase leads and lags, respectively. For each position along the ripple profile, the vertical profile of the mean horizontal velocity is also represented (panels on the R.H.S.).

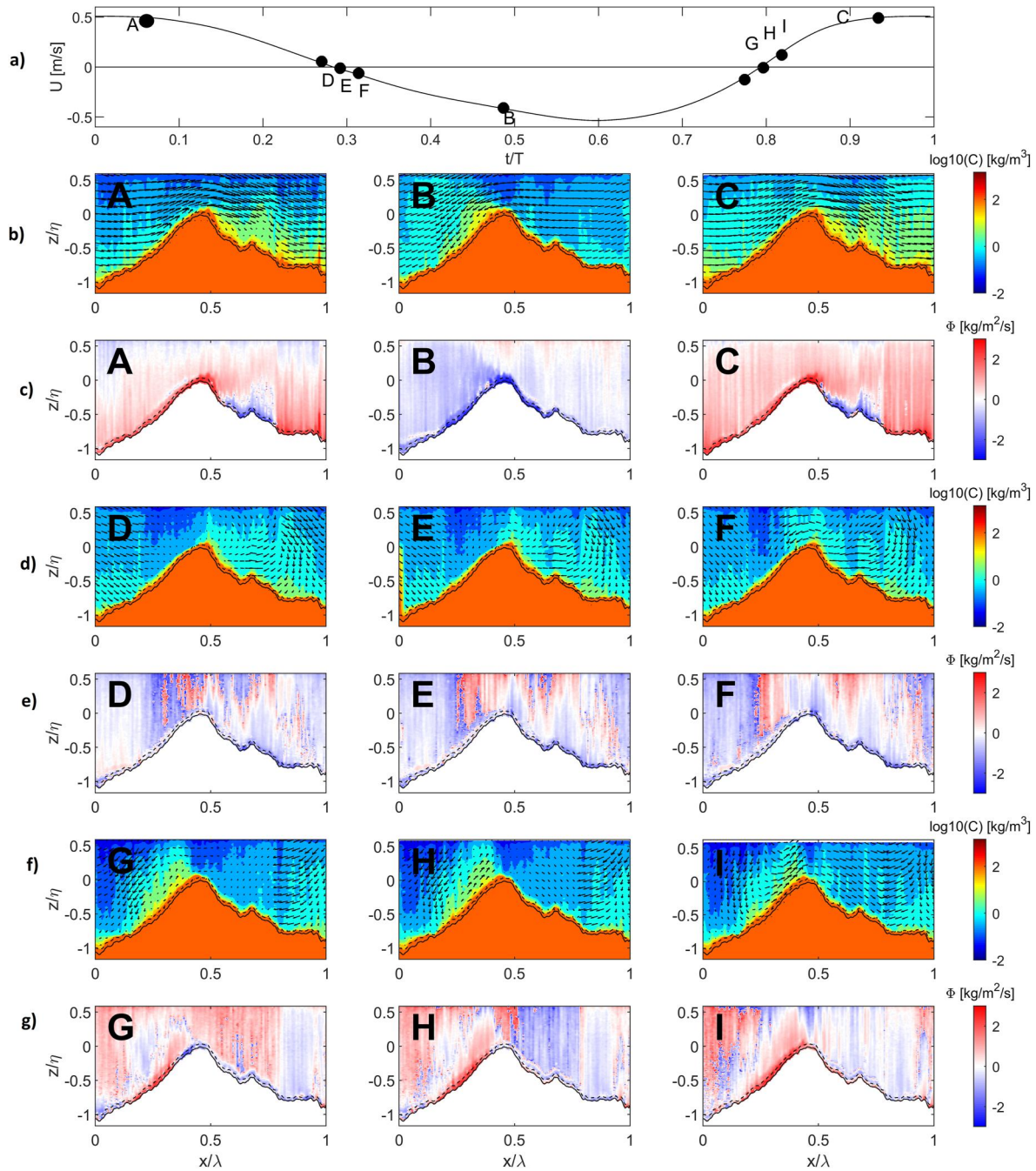


Figure 7. (a) free stream cross-shore velocity (one wave cycle). Then, concentration colorplots (kg/m^3) are superimposed with the velocity fields (m/s) (LTRP data set) at different phase moments (b), (d), and (f). Below, the corresponding cross-shore sediment fluxes ($\text{kg}/\text{m}^2/\text{s}$) are displayed (c), (e), and (g). The solid black line corresponds to the interface between the bedload layer and the non-moving sand bed, and the dashed line is the interface between the bedload and suspension layers. Stoss side is left side of the ripple and lee side is right side. LTRP data have been averaged over eight consecutive waves.

Ripple trough at position A (Figure 9d): Small values of phase leads are observed close to the bed around both FR+ and FR− reversals with maximal values around 10° for FR− and 15° for FR+. These values are similar to those observed at the ripple crest (position C, Figure 9j).

Stoss-side ripple vortex position B (Figure 9f): it can be seen in the colorplot that the FR+ reversal (around phase $t/T = 0.75$) is increasingly leading its free-stream phase when approaching the detected bed level (thick solid black line on the colorplot). This tendency is confirmed by the dashed black curve profile (Figure 9g) revealing

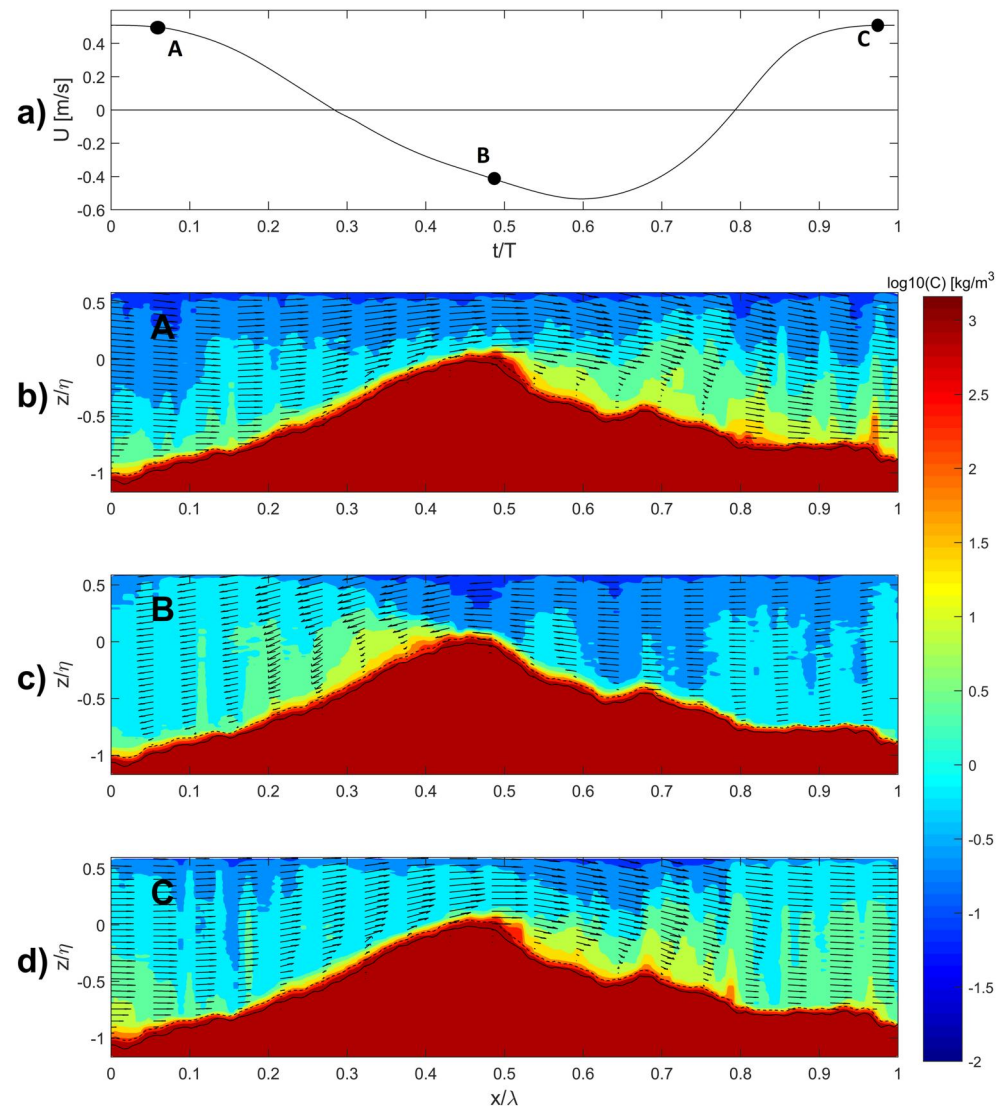


Figure 8. (a) free stream cross-shore velocity (one wave cycle). (b), (c), and (d) Zoom on concentration colorplots and velocity fields (LTRP data set) of sequences A, B and C. Stoss side is left side of the ripple and lee side is right side.

increasing phase lead values in the vicinity of the bed reaching a maximal value of about 80° . For the FR–reversal (around $t/T = 0.33$ in the colorplot), the phase shift is weakly positive and fairly constant with z before becoming weakly negative. The corresponding phase shift (solid black curve on Figure 9g) is therefore close to 0 over the whole profile.

Ripple crest at position C (Figure 9i): At the ripple crest, the velocity field colorplot indicates small values of phase shifts around both FR+ and FR–, in particular, a very low phase lag for FR+, and a value close to 0 for FR–.

Lee-side ripple vortex position D (Figure 9l): in the intrawave velocity colorplot, the FR– reversal is increasingly leading the free-stream phase when approaching the flow bed with much higher phase lead values compared to the one observed around for the FR+ reversal. This is confirmed by the phase shift profiles showing high phase lead values of the curve represented by the solid black line (around 50°) and smaller phase lag values (about 20°) for FR+ (dashed black curve).

Hurthner and Thorne (2011) observed that under velocity-skewed shoaling waves in the ripple vortex regime, FR– and the FR+ flow are also strongly leading the free-stream reversals close to the bed but contrary to here, with a

stronger phase lead value for the FR- at position D compared to FR+ at position B. These differences are attributed to a more intense lee side ripple vortex due to the larger onshore velocity magnitude under velocity skewed waves. In the present acceleration-skewed flow conditions, stronger FR+ phase lead at position B compared to the FR- phase lead at position D is attributed to the stronger flow acceleration during FR+. These strong values of phase leads observed at positions B and D are associated with ripple vortex formation around both flow reversals. It can be noted that these values are much larger than the typical values obtained for turbulent wave boundary layers (usually around 20° , van der A et al., 2011; Fromant et al., 2019). In the present acceleration-skewed waves, only the flow reversal with a nearbed velocity in the same direction as the nearbed vortex velocity direction is leading, with phase lead values above 50° . The significant phase lead values of the FR- and FR+ on the lee- and the stoss-face, respectively, are in agreement with the conclusions of van der Werf et al. (2007) stating that the high phase lead values (i.e., much higher than the typical phase lead values around 20° found for turbulent WBL) are potentially linked with ripple vortex formation. Indeed, the clockwise-rotating vortex formed on the lee side during the FR- reversal tends to reverse the flow earlier than at the free stream height. The equivalent phenomenon is found on the stoss side for the FR+ reversal.

In order to confirm these ripple vortex effects, Figure 9 also shows the mean horizontal velocity profiles at the four considered positions. It can be seen that at positions B and D (Figures 9f and 9l) that the mean current is onshore and offshore directed, respectively, revealing potential effects of the counter-clockwise rotating ripple vortex on the velocity close to the bed on the ripple stoss-side and of the clockwise rotating ripple vortex on the ripple lee-side. The mean signatures of these ripple vortex effects on both ripple faces can be clearly seen in Figure 10 representing the 2C-uw mean velocity field. As expected, the mean current reveals the presence of mean counter rotating vortices on either side of the ripple crest. Similar mean flow signatures were found by Hurther and Thorne (2011) under skewed shoaling waves, with a strong offshore-directed current at the ripple crest. Under our asymmetric wave conditions, such a strong offshore-directed current at the crest is not observed (further discussed in Section 4).

5.3. Sand Concentration Field

Figure 11b shows the intrawave ripple averaged sand concentration field based on the IwP data set. Four distinct suspended sand concentration peaks can be distinguished at phases $t/T = 0.15-0.25$, $t/T = 0.85-0.9$, $t/T = 0.35-0.55$, and $t/T = 0.95-0.05$ corresponding roughly to FR-, FR+, wave trough and wave crest events, respectively.

The two events occurring during the wave crest half-cycle carry more suspended sand than the two events occurring during wave trough. This unbalance between both wave half-cycles is attributed to the more intense acceleration during the FR+ reversal as a consequence of onshore acceleration-skewed waves, which leads to higher bed shear stress values during this very flow reversal. This observation contrasts the case of a velocity-skewed wave for which the highest concentration peak occurs just after the FR- reversal because of the more energetic lee-side ripple vortex generated at the wave crest compared to the less energetic stoss-side ripple vortex generated at the wave trough (due to the smaller velocity trough magnitude). Indeed, for the velocity-skewed wave case, a more energetic sand entrainment occurs at FR- which is subsequently transported in the offshore direction during the wave trough. In turn, for the present acceleration skewed wave condition, the FR+ reversal entrains more sand into suspension (than the FR- reversal), which is subsequently transported onshore during the wave crest. Moreover, no phase lagging effect was seen in the present experiment. Phase lagging is indeed seen to depend on the sand grain size. It is low in presence of coarse sand ($d_{50} = 545 \mu\text{m}$) which exhibit a relatively high settling velocity. In the present experiment, the absence of phase lagging is confirmed by the negligible suspended sand concentration values before the flow reversal events (at $t/T = 0.15-0.25$ and $t/T = 0.85-0.9$) meaning that sand entrained into suspension during a given flow reversal will only be advected during the following wave half-cycle because the entrained sand cloud had sufficient time to settle down to the bed before the following flow reversal event (as the particle entraining event). The net suspended sediment transport rate is therefore onshore oriented in the present coarse sand acceleration skewed wave condition rather than offshore oriented as previously observed for medium sand velocity-skewed oscillatory flows (van der Werf et al., 2007) and for skewed shoaling waves (Hurther & Thorne, 2011).

In order to determine whether the different concentration events observed in Figure 11b are due to local erosion events inducing advective sand transport or due to more uniformly distributed erosion events over the entire ripple length, the local intrawave concentration (LTRP data set) are shown at the 4 specific positions along the ripple profile defined in the previous section. This is represented in Figures 11d-11g, corresponding, respectively, to

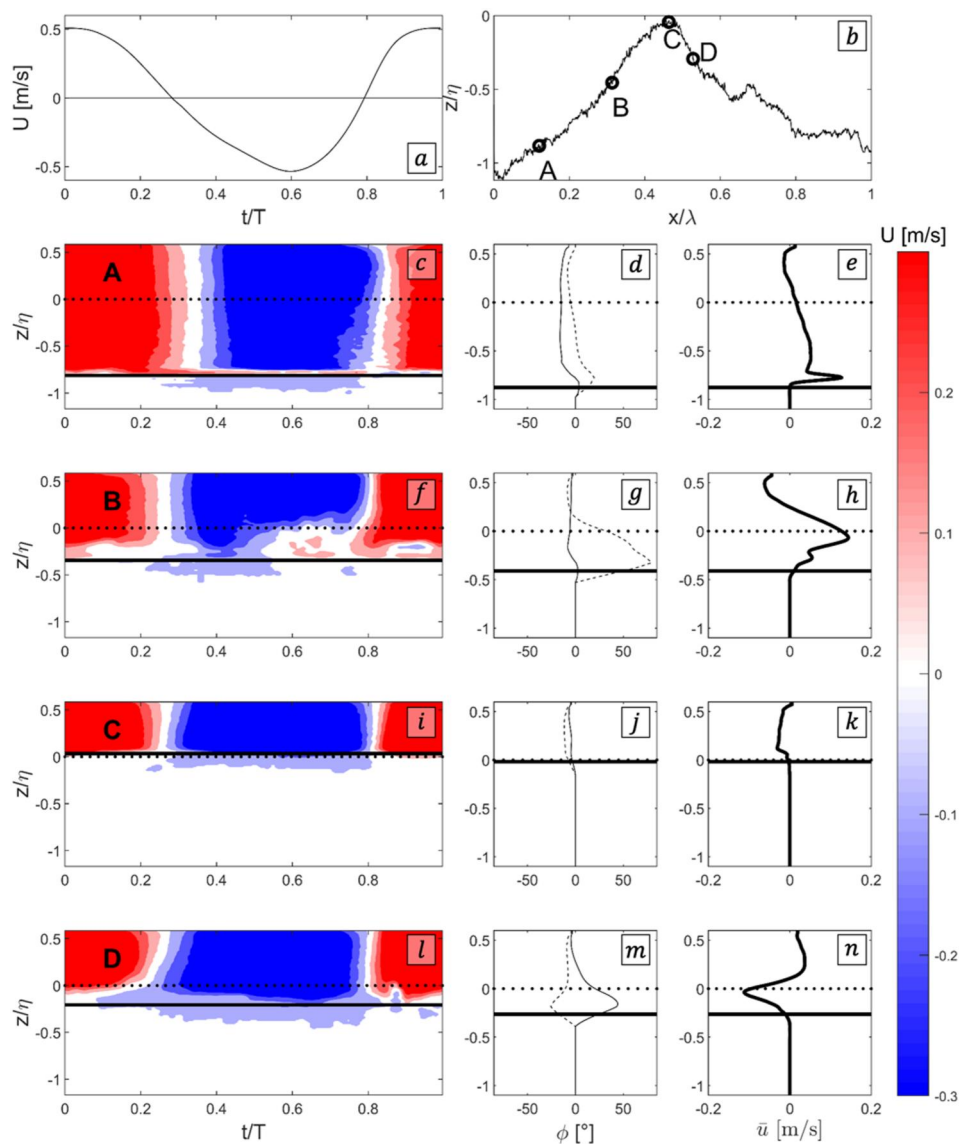


Figure 9. (a) free stream cross-shore velocity (a) and ripple profile with A (ripple trough), B (stoss-face ripple vortex), C (ripple crest) and D (lee-side ripple vortex) locations (b). Intra wave velocity contours (m/s) (c, f, i and l panels), phase shifts ($^{\circ}$) (d, g, j and m panels) and local mean velocity profiles (e, h, k and n panels) are displayed in A, B, C and D positions above the ripple. Phase shifts of the onshore-offshore flow reversal FR- are represented with the solid black line and offshore-onshore flow reversal FR+ are represented with the black dashed line. Local mean velocity profiles are displayed with the thick black line. For both sets of panels, the horizontal thick black solid line corresponds to the local detected bed level and the black dotted line to the ripple crest level (as the origin $z = 0$).

position A at the ripple trough, B at the stoss side ripple vortex position, C at the ripple crest and D at the lee side ripple vortex position.

The concentration peak observed between $t/T = 0.95$ and $t/T = 0.05$ in Figure 11b (at wave crest) can be seen of similar magnitude in panels A, B, C, and D, supporting that the concentration event induced by the wave crest phase has an impact along the whole ripple. This observation suggests a fairly uniformly distributed erosion over the whole ripple length associated with the wave crest event.

The concentration peak at $t/T = 0.35$ – 0.55 in Figure 11b, at wave trough, is less pronounced and less discernible at the four positions because the corresponding suspended sand concentration values are much lower than the wave crest induced suspension concentrations. Furthermore, the low magnitude wave trough events can locally be

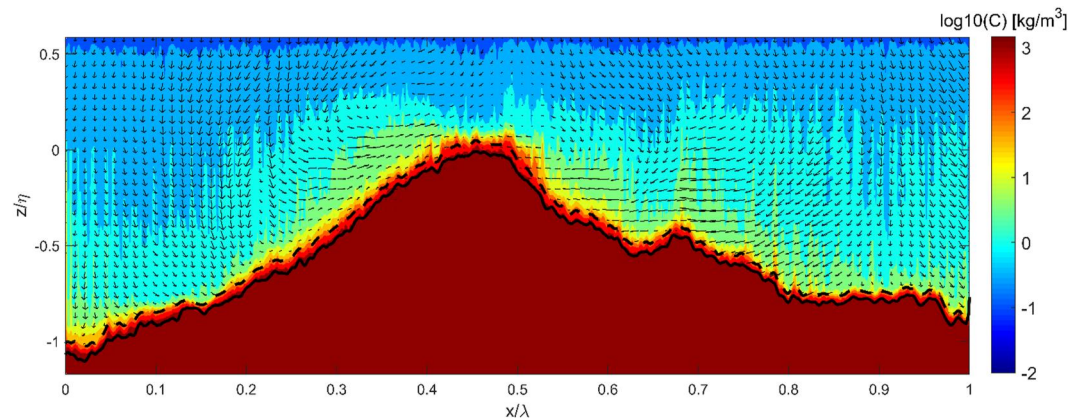


Figure 10. IrP mean concentration and mean 2C-velocity field. The black solid and dashed lines represent the detected bed level and the lower suspension interface, respectively.

superimposed to local advective events of larger magnitude making it difficult to conclude on the spatial uniformity over the ripple length. Nevertheless, it can be said that the wave trough associated event is of lower magnitude in the suspension layer with a potentially uniformly distributed bedload transport over the ripple length.

At position B, two high level concentration peaks occur at $t/T = 0.52$ and $t/T = 0.75$ and one milder peak at $t/T = 0.95$. The last one can be attributed to the uniformly distributed wave crest event whereas the peak at $t/T = 0.52$ can potentially be attributed to suspended sand eroded locally at position D during the FR- reversal and subsequently advected in the offshore direction from position D to A. This sand advection event associated with the clockwise-rotating ripple vortex on the lee side (around position D) moves sand in the offshore direction over a cross-shore distance larger than the distance separating point D from B before it settles down on the ripple stoss side during the offshore half-cycle (as can be partially seen over phases DEFB in the concentration colorplots of Figure 7). The third event at $t/T = 0.75$ in panel B, might be associated to the local sand erosion event induced by the stoss side ripple vortex entrainment at FR- as will be seen in the following panels.

In panel C at the ripple crest, a first distinct suspension concentration peak can be observed at $t/T = 0.95$ – 0.05 attributed to the uniformly distributed wave crest erosion event. A second suspension peak centered at $t/T = 0.35$ is attributed to the local lee side vortex entrainment formed at position D around the FR- reversal and subsequently advected to positions C, B, A. A third suspension peak is observed at $t/T = 0.82$, likely linked to the local stoss side vortex entrainment around position B.

In panel D, a long and high magnitude bedload concentration event is seen between $t/T = 0.85$ and $t/T = 0.35$. The suspension region reveals the presence of three peaks centered around $t/T = 0.88$, 0 and 0.3, respectively. We attribute, respectively, the first to the local erosion event at position B around FR+, the uniformly distributed wave crest erosion event and the local erosion event at position D around FR-.

5.4. Sand Flux Field

In order to determine the contribution to sand transport associated with the previously identified uniform and local sand erosion events, Figure 12 represents, (a) the intrawave ripple averaged sand flux (horizontal component) as bedload (blue curve), as suspension load (gray curve), obtained from IwB and IwS data sets (Figure 6), respectively, and the total sand flux (bedload plus suspension as the black curve). The free-stream velocity signal is also drawn as the dashed gray curve in all intrawave panels of Figure 12. In Figures 12c–12f, the same local intrawave bedload, suspension and total sand flux data (LTRP data set) are shown respectively, for positions A (ripple trough), B (stoss ripple vortex position), C (ripple crest) and D (lee ripple vortex position), along the ripple profile.

It can be seen in Figure 12a that the ripple averaged bedload flux (blue curve) has a larger magnitude than the suspension load flux over the entire wave cycle, except around flow reversals, at $t/T = 0.3$ and $t/T = 0.8$ where both transport modes have a negligible magnitude. The first distinct sand flux event is seen at wave crest ($t/T \approx 0$) in Figure 12a and in all following panels (with a roughly identical magnitude between $3 \times 10^{-4} \text{ m}^2/\text{s}$ and

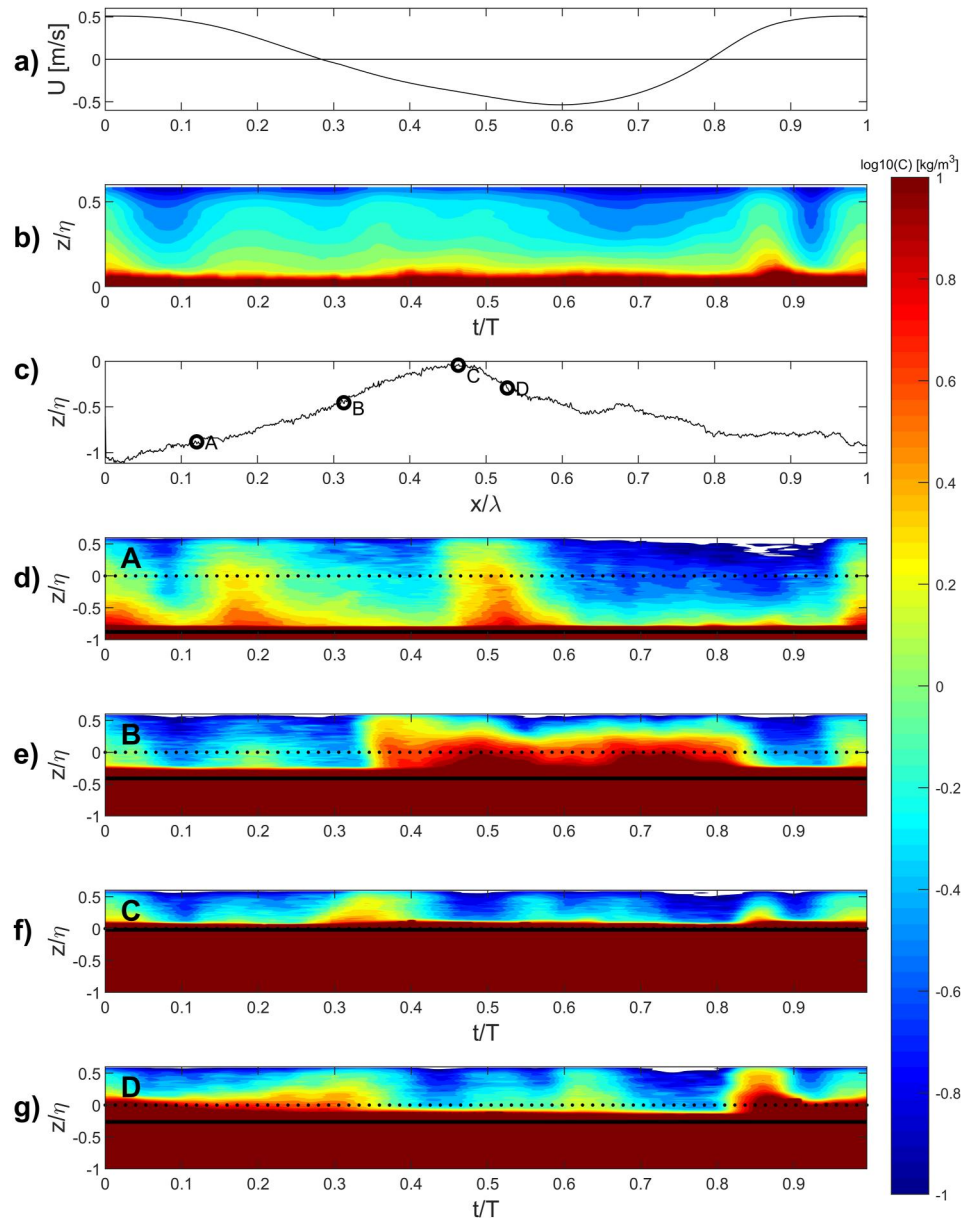


Figure 11. (a) intradune free-stream velocity, (b) intradune ripple averaged (IwP data set) concentration, (c) ripple profile with A (ripple trough), B (stoss-face ripple vortex), C (ripple crest) and D (lee-side ripple vortex) locations. (d) Local intradune concentration (based on IwP data set) at position A, (e) at position B, (f) at position C and (g) at position D. The solid and dotted thick black lines represent the locally detected bed level and the ripple crest level for reference.

$4 \times 10^{-4} \text{ m}^2/\text{s}$) representing the local sand flux dynamics at positions A, B, C and D. This supports a fairly uniformly distributed onshore directed sand transport event over the ripple profile. The contribution of the suspended sand flux is less than 50% of the bedload contribution. The offshore directed sand flux at wave trough ($t/T \approx 0.58$) can be seen in Figure 12a and at positions A (Figure 12c), C (Figure 12e) and D (Figure 12f) but not clearly at position B (Figure 12d) where the flux is already onshore directed. The only potential explanation for this onshore directed sand flux at position B for the phase corresponding to the wave trough in the free-stream signal, is the significant nearbed velocity phase-lead observed previously in Figure 9c (position B) around the FR+ reversal. This phase-lead is seen to provoke a sand flux reversal from offshore to onshore direction at $t/T \approx 0.56$ (Figure 9c), corresponding to the wave trough phase in the free-stream signal.

Local onshore directed sand transport associated with the stoss side ripple vortex entrainment around the FR+ reversal, can be seen at position B for $t/T \approx 0.8$, at position C for $t/T \approx 0.85$ and finally at position D for $t/T \approx 0.9$. The local offshore directed sand transport associated with the lee side ripple vortex around the FR-reversal is seen at position D for $t/T \approx 0.32$, at position C for $t/T \approx 0.35$, at position B, for $t/T \approx 0.4$ and finally at position A for $t/T \approx 0.52$. It appears clearly that the local lee side ripple vortex associated sand flux (in offshore direction) is of lower magnitude than the one generated by the stoss side ripple vortex (in onshore direction). This will supposedly induce a transport unbalance between the two wave half-cycles. As expected from the sand concentration field analysis in the previous Section 5.3, the local ripple vortex induced events contribute to advective sand transport events whereas the sand flux events associated with wave crest and trough are more uniformly distributed over the ripple length.

The four panels on Figure 12g represent the vertical profiles of the net sand flux in horizontal direction at the four positions along the cross-shore ripple profile. The total net sand flux is decomposed into its current induced (time-averaged) and orbital (wave induced) component, following the methodology used in Fromant et al. (2019). This allows to appreciate the relative wave and current contributions to the total cross-shore sand transport rate. The intra-wave components are calculated over 16 consecutive waves. This number of waves is sufficiently high to guaranty a bias error below 10% on the intrawave variable. At the same time, this number of waves is sufficiently low to consider the intrawave variable as local spatially, considering that the ripple migrates over less than 2 cm. The detected bed level (horizontal solid line) and the lower suspension interface position (dotted line), averaged over 16 consecutive waves, are also represented in the four local profile representations of Figure 12g.

It first appears in the net sand flux profiles (Figure 12g) that on either side of the crest, the net sand fluxes at the ripple vortex positions converge toward the crest with similar high magnitudes and a clear bedload dominated transport confirming coarse sand conditions. At the ripple crest position C, the net sand flux is onshore directed with a lower magnitude compared to the values at the ripple vortex positions B and D. Interestingly, this onshore directed sand flux at C is dominated by the wave induced component whereas it is dominated by the current induced component at the two ripple vortex positions and in the ripple trough (position A). The fact that the wave induced sand flux is dominant and onshore directed at the ripple crest suggests that the periodic and more energetic stoss side ripple vortex entrainment is responsible of the onshore directed sand flux at the ripple crest rather than a steady current induced sand transport process. On the contrary, at the two ripple vortex positions (B and D positions in Figure 12g), the mean current vorticity induced by the two ripple vortices (discussed earlier in Figure 10) appear to dominate the total net sand transport rate as a bedload. Another aspect supporting the dominance of the stoss side ripple vortex entrainment for the suspension load is the fact that only at position D, the onshore directed sand flux is a suspension dominated load. This can only result from the energetic stoss side ripple vortex entrainment into suspension of sand from the ripple stoss face, followed by an onshore suspended sand advection during the wave crest half-cycle. This explains why at position D, the suspended sand transport is onshore directed whereas it is offshore directed in the bedload layer due to the lee-side vortex induced mean flow signature (shown above in Figure 9 for position D and in Figure 10). An offshore directed suspended sand flux is not observed at position B because the lee-side ripple vortex entrainment is not sufficiently energetic to entrain sand into suspension at the beginning of the wave trough half-cycle.

Figure 13 represents the sand flux distribution along the cross-shore ripple profile under acceleration-skewed flow conditions. A strong onshore-directed flux can be observed in the bedload layer on the stoss side of the ripple ($t/T = 0.3$), which elongates in a higher onshore patch in the suspension layer ($t/T = 0.45$). On the stoss side, an offshore-directed flux patch can be observed in the bedload layer ($t/T = 0.6$), but its magnitude is lower than the onshore-directed flux patch on the other side of the ripple. Furthermore, the magnitude of the offshore-directed flux patch in the suspension layer ($t/T = 0.42$) is lower than the onshore-directed flux patch in the suspension layer. This strongly highlights the high dynamics of the stoss side vortex, which brings a great quantity of sediment in the onshore direction. This graph pinpoints the imbalance in transport between the stoss side and the lee side of the ripple, highlighting the influence of acceleration-skewed wave condition on sand transport above ripple.

6. Discussion

The present paper focuses on coarse-sand transport processes under asymmetric nearshore waves in the ripple vortex regime. The results have revealed the presence of two ripple vortices over onshore migrating suborbital ripples. The ripple mean shape (shown in Figure 5) exhibits the presence of two elongated ripple troughs with

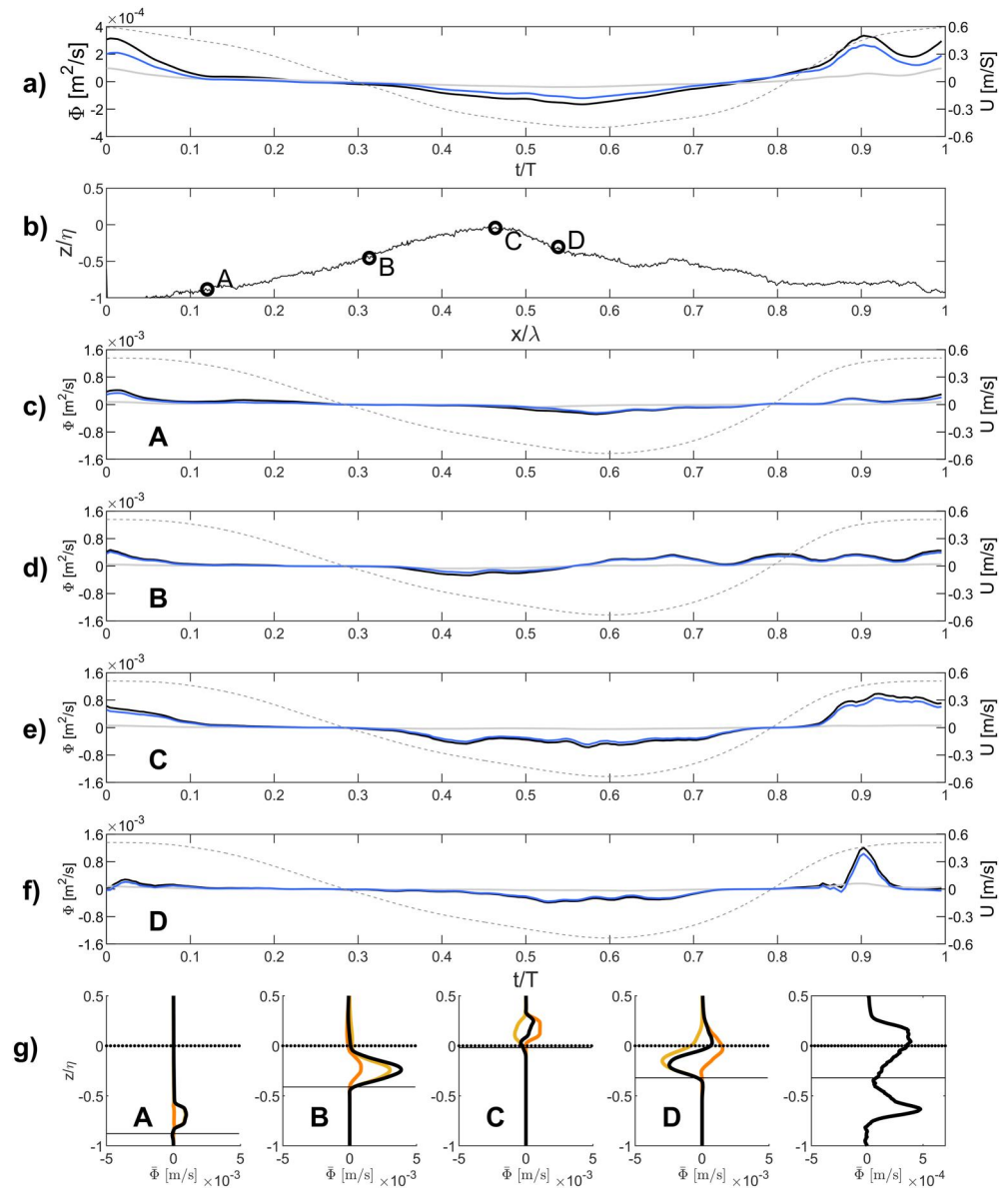


Figure 12. (a) intradaily averaged (IwS data set) flux contributions (dark blue is the total flux, light blue is the bedload flux and gray is the suspended load) and free stream velocity (gray dashed curve), (b) ripple profile with A (ripple trough), B (stoss-face ripple vortex), C (ripple crest) and D (lee-side ripple vortex) locations. (c) Local intradaily flux contribution at position A, (d) at position B, (e) at position C and (f) at position D. Colors are the same as a), with the dashed gray curve representing the free stream cross shore velocity during one wave cycle. (g) Net flux profiles displayed in the ripple trough (A), stoss (B), crest (C) and lee (D). The total flux profile is represented in black, the yellow curve is the current flux component and the orange curve is the orbital flux component. The plain black line is the bed level and the dotted black line represents the ripple crest (referenced at 0).

small humps on either side of the ripple crest and with a slightly steeper lee-side bed slope. Differences in local ripple-vortex induced sand entrainment are found around the flow reversals with a more energetic entrainment around FR+ than around FR-. This is attributed to the stronger flow acceleration (i.e., stronger bed friction) around FR+ at the beginning of the wave crest half-cycle than around FR- during the wave trough half-cycle. We attribute the slightly steeper (offshore) stoss face of the ripple to this stronger (stoss-side ripple vortex induced) sand pick up. Over the entire wave cycle and in the absence of noticeable phase lagging phenomenon, this unbalanced sand entrainment process appears to lead to a stronger onshore directed bedload and suspended sand flux compared to the offshore directed sand flux. How these observations compare to the results found by Wang and

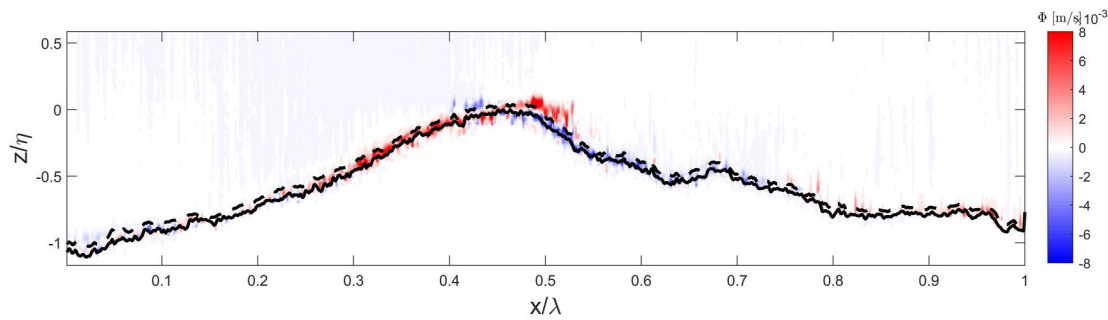


Figure 13. Sand flux distribution along the cross-shore ripple profile (IrP data set) for the present acceleration-skewed flow condition case. Stoss side is the left side of the ripple and lee side is the right side of the ripple. Red patches correspond to onshore-directed flux, and blue patches correspond to the offshore-directed flux.

Yuan (2020) in acceleration skewed oscillatory flows of similar forcing conditions, is discussed in the following paragraph. We compare sand concentration and wave velocity fields (obtained in the present study from the LTRP data set, Figure 7)) with photographs (from Wang and Yuan (2020), Figure 10), at the same four intrawave phases corresponding to wave crest, flow reversal FR-, wave trough and flow reversal FR+. The following main conclusions can be made:

- at FR+, both experiments show more sand entrained into suspension on the stoss face of the ripple, than on the lee side of the ripple at FR-.
- at both flow reversals, for the two experiments, the sand entrainment zones clearly correspond to the zones where the ripple vortices are generated with no other zone of suspended sand. This confirms the leading role played by these local erosion zones in contrast to the more uniformly distributed bedload transport along the ripple profile, occurring at wave crest and trough phases.
- all the suspended load mobilized at the beginning of the given wave half-cycle has sufficient time to settle down to the bed over the corresponding half-cycle period. This supports the absence of phase lagging phenomenon in both coarse sand experiments.
- in both experiments, the local stoss ripple vortex-induced sand entrainment process is followed by a more intense onshore advection of suspended sand at the wave crest compared to a less intense offshore advection of suspended sand at the wave trough.

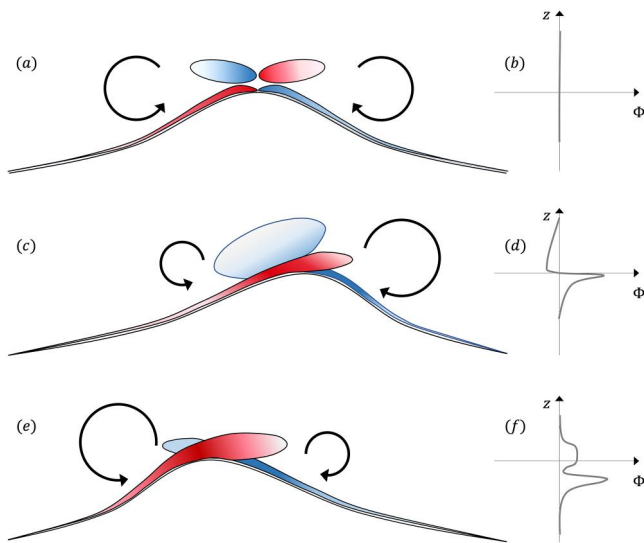


Figure 14. Concluding sketch on sand transport above ripple. First line corresponds to symmetric wave conditions (Salimi-Tarazouj, 2022), second line corresponds to skewed wave conditions (Salimi-Tarazouj, 2022), and third line corresponds to asymmetric wave conditions. The red and blue patches depict the transported sand above the ripple in the onshore (red) and offshore directions (blue). The thick black arrows depict the vortices on both side of the ripple. On the right panels, the typical mean flux profiles under the corresponding hydrodynamic conditions are represented.

These qualitative agreements confirm the predominant role of the same intrawave processes for the coarse sand ripple vortex regime under asymmetric oscillatory flows studied in Wang and Yuan (2020) and the asymmetric nearshore wave experiment studied herein. This result gives further credit to the use of OWT experiments to explore surface wave boundary layer processes in the coarse sand ripple vortex regime above suborbital ripples. This agreement is also important for numerical simulation studies usually reproducing oscillatory boundary layer flows rather than nearshore wave boundary layer flows.

In this study, only one sand grain size was used in the wave flume. It would be interesting to study the influence of grain size on sand transport above ripples. This is why, in the frame of the RIPCOM experiment, some runs were also realized with finer sands, under the same hydrodynamic conditions, in order to observe the influence of grain size on transport above ripples. With finer sand grains, it is likely that a greater effect of phase lag due to the lower settling velocity of the sand may be observed. Moreover, the ratio between suspended and bedload transport might be different than what is observed in the coarse sand case.

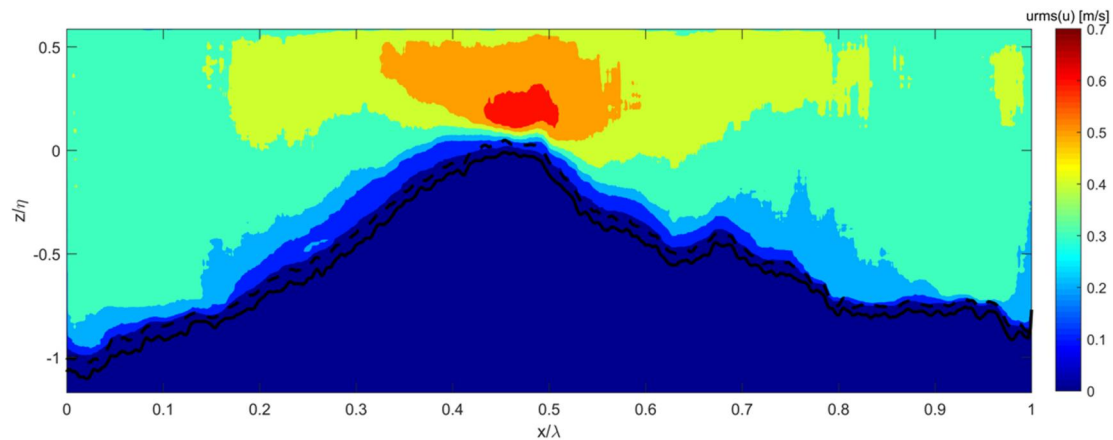


Figure 15. Root mean square values of the cross-shore velocity component above the ripple.

To conclude, Figure 14 shows a sketch summing up the main features of sand transport above ripples under different flow conditions: symmetric, skewed and asymmetric waves. An extended description of sand transport under symmetric and skewed wave conditions can be found in Salimi-Tarazouj, 2022. For the symmetric wave case (first line of Figure 14), the characteristic size of ripple vortices is equal on both sides. It clearly reveals a nearly perfect symmetry of the suspended sand flux patches in opposite direction, around the vertical axis at the ripple crest separating the (symmetric) ripple lee- from the stoss-face crossing the ripple crest. On the contrary, for skewed (second line of Figure 14) and asymmetric (third line of Figure 14) wave conditions, a disequilibrium of vortex size is observed. The consequence of an unbalanced ripple vortex entrainment around the flow reversals generates an unbalanced suspended sand flux in the direction of the wave half-cycle following the more energetic flow reversal. In the case of asymmetric waves, the more energetic ripple vortex entrainment occurs around FR+ which explains the onshore directed net suspended sand flux seen in Figure 12f. In the case of skewed waves and oscillatory flows (Hurther & Thorne, 2011; Salimi et al., 2021), the more energetic ripple vortex entrainment occurs around FR-, which induces an offshore directed net suspended sand flux. Spatially, the zone of largest magnitude of suspended sand flux extends from the position where the ripple vortex subject to the most energetic entrainment is generated, to a region located above the ripple crest on the opposite ripple face. In the case of asymmetric waves, this corresponds to an onshore directed sand flux zone extending from the stoss side ripple vortex to a suspension zone above the ripple crest on the ripple lee face (red patch in Figures 14a, 14c, and 14e). In the case of skewed waves, the zone of largest suspended sand flux corresponds to an offshore directed sand flux zone (blue color) extending from the lee side ripple vortex to a zone above the ripple crest on the ripple stoss side (blue patch in Figure 14b).

The final remark of this section is devoted to an original spatial representation in Figure 15 of the horizontal r.m.s. wave velocity component (orbital component). It is estimated from a time-average over 16 consecutive waves as the IrP representation shown in Figure 13. It appears that an excess of orbital velocity is found in the zone of influence of the ripple vortex entrainment. As for the horizontal sand flux field shown in Figure 13, the non-symmetric distribution of this velocity excess zone around the vertical ripple crest axis with an onshore shift above the ripple lee-face might be representative of the unbalanced ripple vortex entrainment induced by the stoss side ripple vortex around the FR+ flow reversal. Whether a more symmetric velocity excess zone is found for symmetric waves and a non-symmetric one (offshore shifted above the ripple stoss-face) for skewed shoaling waves and oscillatory flows cannot be confirmed here but it might offer a new simple way to check the hydrodynamic performance of numerical simulation codes to reproduce the subtle differences found in the ripple vortex regime for non-linear waves and oscillatory flows.

7. Conclusion

Coarse sand transport processes in the ripple vortex regime have been investigated under asymmetric regular, large-scale nearshore waves using acoustic high-resolution profile measurements of velocities and sand concentrations provided by the ACVP technology. The acoustic measurements allowed thorough analysis of the

intrawave and intra-ripple velocity, concentration and sand flux fields above a migrating ripple, as well as the ripple vortex dynamics. In the light of this study, the following conclusions can be made:

- The studied ripple formed in a wave flume under real asymmetric waves presents features similar to the ripple formed under similar hydrodynamic conditions formed in U-Tube, described in Wang and Yuan (2020), in terms of ripple shape, dimensions, migration speed and net transport rate above the ripple.
- The stoss side vortex entrains more sand in suspension around the FR+ reversal compared to the lee side vortex. Also, the bed shear stress during the FR+ reversal is higher (due to asymmetric flow conditions), and therefore the onshore-directed bedload transport generated by the stoss side vortex is higher than offshore-directed bedload transport generated by the lee side vortex.
- In terms of ripple vortex effects on hydrodynamics, it is worth mentioning that the vortex signature is observed in the mean velocity field measured above the ripple, thus indicating that the hydrodynamic effect of ripple vortices could be considered as mean currents, onshore-directed for the stoss side vortex and offshore-directed for the lee side vortex.
- The mean current induced by the two ripple vortices appears to dominate the total net transport as bedload. The more energetic stoss side vortex creates transport unbalance between both sides of the ripples under asymmetric flow conditions and therefore leads to net onshore directed transport above the ripple.
- Measurements made in the frame of this study are in good adequation with the observations realized under similar hydrodynamic conditions in a U-Tube facility.

Variable name	Symbol
ho	Still water depth (in the flume)
T	Period
H ₀	Wave height
d ₅₀	Median sediment diameter
u ₁	First harmonic velocity amplitude
u ₂	Second harmonic velocity amplitude
D ₀	Orbital diameter
Re	Reynolds number
R	Skewness parameter
ψ	Mobility number
η	Ripple height
λ	Ripple length
u _{max}	Maximum wave velocity over the wave cycle
α	Ratio between first and second harmonics amplitudes
Cb*	Normalized ripple migration speed
Sl	Bed slope

Acknowledgments

The authors wish to thank the staff of CIEMLAB, in particular, Joaquim Sospedra, Oscar Galego, and Ricardo Torres, for their hospitality and hard work during the experimental campaign. This research was funded by the European Community's Horizon 2020 Program through the Integrated Infrastructure Initiative HYDRALAB+COMPLEX (654110). Thanks to ULCO-MTE pole for financial support of N. Fritsch master thesis project. Thanks to ANR project WEST (ANR-20-CE01-0009) for financial support of N. Fritsch PhD project. Comments and remarks of three anonymous reviewers helped to improve the quality of the manuscript for which the authors are thankful.

Data Availability Statement

Data used for this study are available on Zenodo repository Cáceres et al. (2018) <https://zenodo.org/record/1256648> (<http://dx.doi.org/10.5281/zenodo.1256648>).

References

- Amoudry, L. O., Bell, P. S., Thorne, P. D., & Souza, A. J. (2013). Toward representing wave-induced sediment suspension over sand ripples in RANS models. *Journal of Geophysical Research: Oceans*, 118(5), 2378–2392. <https://doi.org/10.1002/jgrc.20188>
- Bagnold, R. A. (1946). Motion of waves in shallow water. Interaction between waves and sand bottoms. *Proceedings of the Royal Society of London A*, 187, 1–18. <https://doi.org/10.1098/rspa.1946.0062>
- Berni, C., Barthélemy, E., & Michallet, H. (2013). Surf zone cross-shore boundary layer velocity asymmetry and skewness: An experimental study on a mobile bed. *Journal of Geophysical Research: Oceans*, 118(4), 2188–2200. <https://doi.org/10.1002/jgrc.20125>
- Bijker, E., van Hijum, W. E., & Vellinga, P. (1976). Sand transport by waves. In *Proc 15th ICCE, Honolulu* (pp. 1149–1167).

- Cáceres, I., Sospedra, J., Coocke, R., Thorne, P., Hurther, D., & Sánchez-Arcilla, A. (2018). Experimental report of the ripple complex experiments (RIPCOM) project. <https://doi.org/10.5281/zenodo.1256648>
- Cheng, H., Liu, C., Li, J., Liu, B., Zheng, Z., Zou, X., et al. (2018). Experimental study of aeolian sand ripples in a wind tunnel. *Earth Surface Processes and Landforms*, *43*(1), 312–321. <https://doi.org/10.1002/esp.4246>
- Davies, A. G., & Thorne, P. D. (2005). Modeling and measurement of sediment transport by waves in the vortex ripple regime. *Journal of Geophysical Research*, *110*(C5), C05017. <https://doi.org/10.1029/2004JC002468>
- Davies, A. G., & Villaret, C. (1997). Oscillatory flow over rippled beds: Boundary layer structure and wave-induced Eulerian drift. *International Series on Advances in Fluid Mechanics*, *10*, 215–254.
- Earnshaw, H., & Greated, C. (1998). Dynamics of ripple bed vortices. *Experiments in Fluids*, *25*(3), 265–275. <https://doi.org/10.1007/s003480050229>
- Foster, D. L., Bowen, A. J., Holman, R. A., & Natoo, P. (2006). Field evidence of pressure gradient induced incipient motion. *Journal of Geophysical Research*, *111*(C5), C05004. <https://doi.org/10.1029/2004JC002863>
- Fromant, G., Hurther, D., van der Zanden, J., van der A, D. A., Cáceres, I., O'Donoghue, T., & Ribberink, J. S. (2019). Wave boundary layer hydrodynamics and sheet flow properties under large-scale plunging-type breaking waves. *Journal of Geophysical Research: Oceans*, *124*(1), 75–98. <https://doi.org/10.1029/2018JC014406>
- Fromant, G., Mieras, R. S., Revil-Baudard, T., Puleo, J. A., Hurther, D., & Chauchat, J. (2018). On bedload and suspended load measurement performances in sheet flows using acoustic and conductivity profilers. *Journal of Geophysical Research: Earth Surface*, *123*(10), 2546–2562. <https://doi.org/10.1029/2017JF004560>
- Guta, H., Hurther, D., & Chauchat, J. (2022). Bedload and concentration effects on turbulent suspension properties in heavy particle sheet flows. *Journal of Hydraulic Engineering, American Society of Civil Engineers*, *148*(7), 04022012. [https://doi.org/10.1061/\(ASCE\)HY.1943-7900.0001988](https://doi.org/10.1061/(ASCE)HY.1943-7900.0001988)
- Hurther, D., & Thorne, P. D. (2011). Suspension and near-bed load sediment transport processes above a migrating, sand-rippled bed under shoaling waves. *Journal of Geophysical Research*, *116*(C7), C07001. <https://doi.org/10.1029/2010JC006774>
- Hurther, D., Thorne, P. D., Bricault, M., Lemmin, U., & Barnoud, J. M. (2011). A multi-frequency Acoustic Concentration and Velocity Profiler (ACVP) for boundary layer measurements of fine-scale flow and sediment transport processes. *Coastal Engineering*, *58*(7), 594–605. <https://doi.org/10.1016/j.coastaleng.2011.01.006>
- King, D. B. (1991). *Studies in oscillatory flow bedload sediment transport. PhD Thesis* (pp. 184). Univ of California.
- Kranenburg, W. M., Ribberink, J. S., Uittenbogaard, R. E., & Hulscher, S. J. M. H. (2012). Net currents in the wave bottom boundary layer: On waveshape streaming and progressive wave streaming. *Journal of Geophysical Research*, *117*(F3), F03005. <https://doi.org/10.1029/2011JF002070>
- Longuet-Higgins, M. S. (1953). Mass transport in water waves. *Philosophical Transactions of the Royal Society of London - Series A: Mathematical and Physical Sciences*, *245*535–245581. <https://doi.org/10.1098/rsta.1953.0006>
- Malarkey, J., & Davies, A. G. (2002). Discrete vortex modelling of oscillatory flow over ripples. *Ocean Research*, *24*(3), 127–145. [https://doi.org/10.1016/S0141-1187\(02\)00035-4](https://doi.org/10.1016/S0141-1187(02)00035-4)
- Moate, B. D., Thorne, P. D., & Cooke, R. D. (2016). Field deployment and evaluation of a prototype autonomous two-dimensional acoustic backscatter instrument: The Bedform and Suspended Sediment Imager (BASSI). *Continental Shelf Research*, *112*, 78–91. <https://doi.org/10.1016/j.csr.2015.10.017>
- Naqshband, S., Hoitink, A. J. F., McElroy, B., & Hurther, D. H. S. (2017). A sharp view on river dune transition to upper stage plane bed. *Geophysical Research Letters*, *44*(22), 11437–11444. <https://doi.org/10.1002/2017GL075906>
- Naqshband, S., Ribberink, J. S., Hurther, D., & Hulscher, S. J. M. H. (2014). Bed load and suspended load contributions to migrating sand dunes in equilibrium. *Journal of Geophysical Research: Earth Surface*, *119*(5), 1043–1063. <https://doi.org/10.1002/2013JF003043>
- Nichols, C. S., & Foster, D. L. (2007). Full-scale observations of wave-induced vortex generation over a rippled bed. *Journal of Geophysical Research*, *112*(C10), C10015. <https://doi.org/10.1029/2006JC003841>
- Nielsen, P. (1988). Three simple models of wave sediment transport. *Coastal Engineering*, *12–1*(1), 43–62. [https://doi.org/10.1016/0378-3839\(88\)90014-2](https://doi.org/10.1016/0378-3839(88)90014-2)
- Nielsen, P. (1992). *Coastal bottom boundary layers and sediment transport*. World Scientific. Retrieved from <https://books.google.fr/books?id=53MQC15q54wC>
- Nielsen, P., Svendsen, I., & Staub, C. (1978). Onshore-offshore sediment movement on a beach. *Coastal Engineering Proceedings*, *1*(16), 87. <https://doi.org/10.9753/ficce.v16.87>
- O'Donoghue, T., Doucette, J. S., van der Werf, J. J., & Ribberink, J. S. (2006). The dimensions of sand ripples in full-scale oscillatory flows. *Coastal Engineering*, *53*(12), 997–1012. <https://doi.org/10.1016/j.coastaleng.2006.06.008>
- O'Donoghue, T., & Wright, S. (2004). Flow tunnel measurements of velocities and sand flux in oscillatory sheet flow for well-sorted and graded sands. *Coastal Engineering*, *51*(11–12), 1163–1184. <https://doi.org/10.1016/j.coastaleng.2004.08.001>
- Revil-Baudard, T., Chauchat, J., Hurther, D., & Barraud, P. (2015). Investigation of sheet-flow processes based on novel acoustic high-resolution velocity and concentration measurements. *Journal of Fluid Mechanics*, *767*, 1–30. <https://doi.org/10.1017/jfm.2015.23>
- Ribberink, J. S., & Al-Salem, A. A. (1995). Sheet flow and suspension of sand in oscillatory boundary layers. *Coastal Engineering*, *25*(3–4), 205–225. [https://doi.org/10.1016/0378-3839\(95\)00003-T](https://doi.org/10.1016/0378-3839(95)00003-T)
- Ribberink, J. S., van der Werf, J. J., O'Donoghue, T., & Hassan, W. N. M. (2008). Sand motion induced by oscillatory flows: Sheet flow and vortex ripples. *Journal of Turbulence*, *9*, 1–32. <https://doi.org/10.1080/14685240802220009>
- Ruessink, B. G., Ramaekers, G., & van Rijn, L. C. (2012). On the parameterization of the free-stream non-linear wave orbital motion in nearshore morphodynamic models. *Coastal Engineering*, *65*, 56–63. <https://doi.org/10.1016/j.coastaleng.2012.03.006>
- Salimi-Tarazouj, A. (2022). Two-phase modelling of sand ripple dynamics in oscillatory flow.
- Salimi-Tarazouj, A., Cheng, Z., Hsu, T. J., Traykovski, P., & Chauchat, J. (2020). A Eulerian two-phase modeling of ripple dynamics. In *Ocean sciences meeting 2020, AGU*.
- Salimi-Tarazouj, A., Hsu, T.-J., Traykovski, P., Cheng, Z., & Chauchat, J. (2021). A numerical study of onshore ripple migration using a Eulerian two-phase model. *Journal of Geophysical Research: Oceans*, *126*(2), e2020JC016773. <https://doi.org/10.1029/2020JC016773>
- Sato, S., & Horikawa, K. (1986). Laboratory study on sand transport over ripples due to asymmetric oscillatory flows. *Coastal Engineering Proceedings*, *1*(20), 109. <https://doi.org/10.9753/ficce.v20.10>
- Scandura, P., Vittori, G., & Blondeaux, P. (2000). Three-dimensional oscillatory flow over steep ripples. *Journal of Fluid Mechanics*, *412*, 355–378. <https://doi.org/10.1017/S0022112000008430>
- Shimamoto, T. (2016). *Beach recovery and studies in accretive sediment transport*. School of Civil Engineering. <https://doi.org/10.14264/uql.2016.301>

- Shimamoto, T. (2016). *Beach recovery and studies in accretive sediment transport*. PhD Thesis at the University of Queensland. Retrieved from <https://espace.library.uq.edu.au/view/UQ:387531>
- Sleath, J. (1984). Measurements of mass transport over a rough bed. *Coastal Engineering Proceedings*, 1(19), 78. <https://doi.org/10.9753/icce.v19.78>
- Sleath, J. F. A. (1999). Conditions for plug formation in oscillatory flow. *Continental Shelf Research*, 19(13), 1643–1664. [https://doi.org/10.1016/S0278-4343\(98\)00096-X](https://doi.org/10.1016/S0278-4343(98)00096-X)
- Thorne, P. D., Davies, A. G., & Bell, P. S. (2009). Observations and analysis of sediment diffusivity profiles over sandy rippled beds under waves. *Journal of Geophysical Research*, 114(C2), C02023. <https://doi.org/10.1029/2008JC004944>
- Thorne, P. D., & Hanes, D. M. (2002). A review of acoustic measurement of small-scale sediment processes. *Continental Shelf Research*, 22(4), 603–632. [https://doi.org/10.1016/S0278-4343\(01\)00101-7](https://doi.org/10.1016/S0278-4343(01)00101-7)
- Thorne, P. D., & Hurther, D. (2014). An overview on the use of backscattered sound for measuring suspended particle size and concentration profile in non-cohesive inorganic sediment transport studies. *Continental Shelf Research*, 73, 97–118. <https://doi.org/10.1016/j.csr.2013.10.017>
- Thorne, P. D., Hurther, D., Cooke, R. D., Cáceres, I., Barraud, P. A., & Sánchez-Arcilla, A. (2018). Developments in acoustics for studying wave-driven boundary layer flow and sediment dynamics over rippled sand-beds. *Continental Shelf Research*, 166, 119–137. <https://doi.org/10.1016/j.csr.2018.07.008>
- Trowbridge, J., & Madsen, O. S. (1984). Turbulent wave boundary layers: 1. Model formulation and first-order solution. *Journal of Geophysical Research*, 89(C5), 7989–7997. <https://doi.org/10.1029/JC089iC05p07989>
- Van der, A. D., O'Donoghue, T., Davies, A., & Ribberink, J. (2011). Experimental study of the turbulent boundary layer in acceleration-skewed oscillatory flow. *Journal of Fluid Mechanics*, 684, 251–283. <https://doi.org/10.1017/jfm.2011.300>
- Van der, A. D., Ribberink, J. S., van der Werf, J. J., O'Donoghue, T., Buijsrogge, R. H., & Kranenburg, W. M. (2013). Practical sand transport formula for non-breaking waves and currents. *Coastal Engineering*, 76, 26–42. <https://doi.org/10.1016/j.coastaleng.2013.01.007>
- Van der Werf, J. J., Doucette, J. S., O'Donoghue, T., & Ribberink, J. S. (2007). Detailed measurements of velocities and suspended sand concentrations over full-scale ripples in regular oscillatory flow. *Journal of Geophysical Research*, 112(F2), F02012. <https://doi.org/10.1029/2006JF000614>
- Van der Werf, J. J., Magar, V., Malarkey, J., Guizien, K., & O'Donoghue, T. (2008). 2DV modelling of sediment transport processes over full-scale ripples in regular asymmetric oscillatory flow. *Continental Shelf Research*, 28(8), 1040–1056. <https://doi.org/10.1016/j.csr.2008.02.007>
- Van der Werf, J. J., Ribberink, J. S., O'Donoghue, T., & Doucette, J. S. (2006). Modelling and measurement of sand transport processes over full-scale ripples in oscillatory flow. *Coastal Engineering*, 53(8), 657–673. <https://doi.org/10.1016/j.coastaleng.2006.02.002>
- Van der Zanden, K., van der A. D. A., Hurther, D., Cáceres, I., O'Donoghue, T., & Ribberink, J. S. (2017). Suspended sediment transport around a large scale laboratory breaker bar. *Coastal Engineering*, 125, 51–69. <https://doi.org/10.1016/j.coastaleng.2017.03.007>
- Villard, P. V., Osborne, P. D., & Vincent, C. E. (2000). Influence of wave groups on SSC patterns over vortex ripples. *Continental Shelf Research*, 20(17), 2391–2410. [https://doi.org/10.1016/S0278-4343\(99\)00068-0](https://doi.org/10.1016/S0278-4343(99)00068-0)
- Wang, D., & Yuan, J. (2018). Bottom-slope-induced net sediment transport rate under oscillatory flows in the rippled-bed regime. *Journal of Geophysical Research: Oceans*, 123(10), 7308–7331. <https://doi.org/10.1029/2018JC013810>
- Wang, D., & Yuan, J. (2020). An experimental study of net sediment transport rate due to acceleration-skewed oscillatory flows over rippled seabeds. *Coastal Engineering*, 155, 103583. <https://doi.org/10.1016/j.coastaleng.2019.103583>
- Widberg, P. L., & Harris, C. K. (1994). Ripple geometry in wave-dominated environments. *Journal of Geophysical Research*, 99(C1), 775–789. <https://doi.org/10.1029/93JC02726>
- Zhang, J., Salimi-Tarajouz, A., Mathieu, A., Hsu, T. J., & Michael, H. (2022). A numerical study on wave-driven ripple migration and benthic flux. *THESIS conference proceedings*.
- Zomer, J. Y., Naqshband, S., Vermeulen, B., & Hoitink, A. J. F. (2021). Rapidly migrating secondary bedforms can persist on the lee of slowly migrating primary river dunes. *Journal of Geophysical Research: Earth Surface*, 126(3), e2020JF005918. <https://doi.org/10.1029/2020JF005918>